Thomas Tveit Ulstein

Aspects of Flow and Heat Transfer in Finned Tube Bundles

Master's thesis in Energy and Environmental Engineering
Supervisor: Erling Næss
June 2019

Master's thesis

NTNU
Norwegian University of Science and Technology
Faculty of Engineering
Department of Energy and Process Engineering

NTNU
Norwegian University of
Science and Technology

Thomas Tveit Ulstein

Aspects of Flow and Heat Transfer in Finned Tube Bundles

Master's thesis in Energy and Environmental Engineering
Supervisor: Erling Næss
June 2019

Norwegian University of Science and Technology
Faculty of Engineering
Department of Energy and Process Engineering

NTNU
Norwegian University of
Science and Technology

Abstract

The heat transfer experiment was performed in a specialized rig, with hot air as a substitute for exhaust gas. Both heat transfer and pressure drop were investigated for a staggered tube array consisting of elliptical tubes with rectangular fins. The Reynolds number was based on the minimum flow area and the hydraulic diameter of the tubes, and was varied from 5 500 to 38 600. Through a data reduction procedure, correlations for both heat transfer and pressure drop were found in the form of Euler-Reynolds and Nusselt-Reynolds equations, respectively.

The Euler-Reynolds equations were Eu = $13.910\text{Re}^{-0.28}$ for the large orifice and Eu = $19.129\text{Re}^{-0.31}$ for the small orifice. These show a good agreement with published correlations, and the exponents are well within the range of previous work. The Nusselt-Reynolds equations were Nu = $0.576\text{Re}^{0.44}$ for the large orifice and Nu = $0.576\text{Re}^{0.36}$ for the small orifice. The Nusselt-Reynolds correlations show some deviation compared to previous work. This deviation was thought to be the result of fouling inside the tubes, and an attempt to quantify the fouling factor was made. Accounting for this fouling factor showed that a fouling factor of 0.0004 - 0.0007 $\text{m}^2\text{K/W}$ would correlate the results nicely with previous work.

To investigate the risk of excessive tube vibration in compact heat exchanger units, a Fortran 90 program was created. The program returns the the natural frequencies and corresponding mode shapes of a finned tube with intermediate supports. In addition to this, it assesses the risk of vortex induced vibration, fluid-elastic instability, turbulent buffetting and acoustic resonance, based on input chosen by the user. To test the program, it was run with the same input as two previously worked examples from the literature, and managed to replicate the results well.

Sammendrag

Varmeovergangseksperimentet ble gjennomført i en spesialisert rigg, hvor oppvarmet luft ble brukt som en erstatning for eksosgass. Både varmeovergang og trykkfall ble undersøkt for elliptiske rør med rektangulære finner, arrangert i forskjøvne rekker. Reynoldstallet ble beregnet ut fra det minste strømningsarealet og rørenes hydrauliske diameter, og varierte mellom 5 500 og 38 600. Gjennom en datareduksjonsprosedyre ble korrelasjoner for både trykkfall og varmeovergang funnet i form av henholdsvis Euler-Reynolds og Nusselt-Reynolds korrelasjoner.

Euler-Reynolds korrelasjonene var Eu = 13,910$\mathrm{Re}^{-0,28}$ for den største blendeskiven, og Eu = 19,129$\mathrm{Re}^{-0,31}$ for den minste blendeskiven. Disse korrelasjonene stemmer godt overens med tidligere publisert forskning, hvor Euler-Reynolds ligningene var innenfor spekteret av tidligere resultater. Nusselt-Reynolds korrelasjonene var Nu = 0,576$\mathrm{Re}^{0,44}$ for den største blendeskiven, og Nu = 0,576$\mathrm{Re}^{0,36}$ for den minste blendeskiven. Disse avviker fra tidligere resultater. Dette avviket ble antatt å være et resultat av begroing på innsiden av rørene, og denne begroingsfaktoren ble forsøkt tallfestet. Det viste seg at ved å legge til en begroingsfaktor på 0,0004-0,0007 m^2K/W så samsvarte resultatene med tidligere arbeid.

For å undersøke risikoen for ødeleggende rørvibrasjoner i kompakte varmevekslere, ble et Fortran 90 program laget. Programmet returnerer de naturlige svingefrekvensene og modusformene til et finnet rør med mellomliggende støtter. I tillegg blir risikoen for virvelindusert vibrasjon, fluidelastisk ustabilitet, turbulensindusert eksitasjon og akustisk resonans vurdert, basert på inngangsverdier som brukeren selv velger. For å teste programmet ble det kjørt med samme inngangsverdier som to tidligere eksempler fra litteraturen, og gjenskapte resultatene fra eksemplene godt.

Acknowledgement

I would like to express my sincere thanks to my supervisor Erling Næss for his support during the process of writing this thesis. Thank you for your always having an open door and for many good conversations.

Thank you to all the staff working in the lab for always being on hand when needed.

Contents

List of Tables

List of Figures

Nomenclature

Latin notation

Symbol	Parameter	Unit
A	Area	m^2
A_i	Inner tube area	m^2
A_o	Outer tube area	m^2
A_f	Fin area	m^2
A_{bt}	Bare tube area	m^2
c	Fin spacing	m
c_0	Speed of sound	m/s
c_{eff}	Effective speed of sound	m/s
c_f	Fanning type friction coefficient	[-]
c_p	Specific heat capacity, constant pressure	kgm^2/s^2K
c_v	Specific heat capacity, constant volume	kgm^2/s^2K
C	Discharge coefficient	[-]
C_L	Fluctuating lift coefficient	[-]
d	Orifice diameter	m
D_b, D	Bare tube diameter	m
D_e	Effective diameter	m
D_f	Finned diameter	m
D_h	Hydraulic diameter	m
D_i	Inner tube diameter	m
D_o	Outer tube diameter	m
D_r	Geometrical parameter for finned tubes	m
D_{vol}	Volumetrically based effective diameter	m
E	Young's modulus	kg/ms^2
F	Fin parameter for calculating second moment of area	[-]
f	Frequency	1/s
f_a	Acoustic resonance frequency	1/s
f_n	Natural frequency	1/s
f_{tb}	Turbulent buffeting frequency	1/s
f_v	Vortex shedding frequency	1/s
F_L	Lift force	kgm/s
F_{min}	Open area between finned tubes	m^2
h	Convective heat transfer coefficient	W/m^2K
h_f	Fin height	m
H_s, H_r	Frequency response functions	[-]
I	Second moment of inertia	m^4
I_0, I_1	First order modified Bessel function	[-]
I_{eff}	Effective second moment of area	m^4

k	Thermal conductivity	W/mK
K	Fluid-elastic instability constant	[-]
K_0, K_1	Second order modified Bessel function	[-]
L	Support to support tube length	m
L	Characteristic length	m
m	Mass per unit length	kg/m
N	Number of spans	[-]
N_f	Fin density	fins/m
N_L	Number of tubes in lateral direction	[-]
N_T	Number of tubes in transverse direction	[-]
p_1	Pressure upstream of orifice	kg/ms^2
p_2	Pressure downstream of orifice	kg/ms^2
$p_{t.s.}$	Pressure in test section	kg/ms^2
P	Pressure	kg/ms^2
P_l	Longitudinal tube pitch	m
P_t	Transverse tube pitch	m
Q, q	Heat transfer rate	W
$q_m, \dot{m}$	Mass flow rate	kg/s
R	Specific gas constant	m^2/s^{2}K
R_f	Fouling factor	m^{2}K/W
r_0, r_1, r_2	Tube radiuses	m
s_f	Fin pitch	m
t	Fin thickness	m
$\bar{T_{t.s.}}$	Average test section temperature	K
U	Overall heat transfer coefficient	W/m^{2}K
U_{max}	Maximum test section velocity	m/s
V, U_p	Pitch velocity	m/s
V_{cr}	Critical pitch velocity	m/s
$\dot{V}$	Volume flow	m^3/s
W	Heat exchanger dimension normal to the flow	m
$W_{t.s.}$	Test section width	m
Y	Vibration amplitude	m
Y_{max}	Maximum amplitude	m
$Y_{max,r.m.s.}$	Maximum root mean square amplitude	m

Greek notation

Symbol	Parameter	Unit
β	Orifice to tube diameter ratio	[-]
β_n	Natural frequency coefficient	[-]
δ	Mass damping parameter	[-]
Δ	Change in pressure over orifice	[-]
ϵ	Expansibility factor	[-]
ϵ_g	Void fraction	[-]
η_f	Fin efficiency	[-]
θ_b	Temperature difference	K

ζ	Damping ratio	[-]
Θ	Phase angle	rad
κ	Heat capacity ratio	[-]
κ	Mode shape eigenvalue	[-]
λ	Vibration shape constant	[-]
μ	Dynamic viscosity	kg/ms
ν	Kinematic viscosity	m^2/s
π	Ratio of circumference to diameter	[-]
ρ	Mass density of fluid	kg/m^3
ρ_o	External fluid density	kg/m^3
ρ_{tube}	Mass density of tube material	kg/m^3
σ	Tube volume fraction	[-]
ϕ	Mode shape	m
ψ	Mode shape	m

Dimensionless numbers

$$Euler\ number: \qquad Eu = \frac{\Delta P}{N_L \frac{1}{2} \rho V^2} \tag{1}$$

$$Nusselt\ number: \qquad Nu = \frac{hD}{k} \tag{2}$$

$$Prandtl\ number: \qquad Pr = \frac{\mu c_p}{k} \tag{3}$$

$$Reynolds\ number: \qquad Re = \frac{\rho V D}{\mu} \tag{4}$$

$$Strouhal\ number: \qquad St = \frac{fD}{V} \tag{5}$$

1 Introduction

1.1 Background

The Intergovernmental Panel on Climate Change's 2018 report titled "Special Report on Global Warming of 1.5 °C" states that if the global temperature rise is to be limited to only 1.5 °C, drastic steps must be made [8]. These changes would entail, among other things, reducing CO_2 emissions associated with power production. One way of achieving this is to enhance the efficiency of already existing power plants.

An excellent way to increase energy efficiency is to better utilize the heat in exhaust gases from gas turbines. One method in achieving this is through combined cycles, where a bottom cycle is combined with the gas turbine and reuses the exhaust heat. In this way, the energy that otherwise would have gone to waste can be transferred to other means. By doing this, less gas is needed to produce the same amount of power, and therefore the efficiency will increase.

The usage of such combined cycles is less common offshore than offshore. This is due to the strict weight and size restrictions associated with offshore production. Because of this, waste heat recovery units for offshore usage must be efficient in both weight and size. Such solutions are often susceptible to damage from excessive tube vibrations due to the limited space available inside the heat exchanger. This vibration may cause excessive wear and tear, and in some cases, cause breakdowns to occur. Because of this, thorough considerations of these factors are necessary for optimal design of compact waste heat recovery units.

1.2 Objective

The objective of this thesis is to investigate the flow and heat transfer characteristics of a finned tube bundle. Such thermal-hydraulic characteristics are essential to know when designing compact heat exchanger units. Pressure drop, heat transfer, and tube vibration are all design aspects which need to be assessed for compact waste heat recovery units.

The investigation into these characteristics was done in two parts. Firstly, an experiment on a finned tube array was carried out on a bundle of elliptical tubes with rectangular fins.

The measurements gathered from this experiment were used to develop correlations for both heat transfer and pressure drop for the prediction of the thermal-hydraulic behavior of the tube bundle. Secondly, a vibration response prediction program was created. This program aimed to investigate the risk of excessive vibration of finned tubes. The program was created so that the user may input parameters of their choosing, and can investigate tube geometries of their choice. Due to time constraints and the complexity of the calculations, vibration in U-bend regions of heat exchangers was not included in the program.

Both the thermal-hydraulic characteristics and risk of excessive vibration are critical design parameters that are all important factors when designing compact waste heat recovery units.

2 Theory

The purpose of this chapter is to provide relevant background theory for convection, conduction, overall heat transfer coefficients and finned tubes, as well as introducing important dimensionless numbers. Also, the chapter presents equations, parameters, and mechanisms that will serve as the theoretical background of the vibration response prediction program. Parts of 2.1, 2.2, 2.3 and 2.4, excluding 2.4.3, have been reused and modified from the author's earlier project thesis.

2.1 Dimensionless numbers

Euler number

The Euler number, Eu, expresses the ratio of the local pressure drop to the kinetic energy of the flow, per unit volume. An Euler number of 1 corresponds to perfect, frictionless flow. In the context of these experiments, the Euler number has to be adjusted for the number of tube rows.

$$Eu = \frac{\Delta P}{N_L \frac{1}{2} \rho V^2} \tag{2.1}$$

Where ΔP is the pressure drop, N_L is the number of longitudinal tube rows, ρ is the fluid density, and V is the fluid velocity.

Nusselt number

The Nusselt number, Nu, expresses the ratio of convective to conductive heat transfer normal to the boundary.

$$Nu = \frac{hL}{k_f} \tag{2.2}$$

Where h is the local convection coefficient, L is the characteristic length, and k_f is the fluid thermal conductivity.

Prandtl number

The Prandtl number, Pr, is the ratio of the momentum diffusivity to the thermal diffusivity. For small Prandtl numbers, the momentum diffusivity dominates, and for large Prandtl numbers the thermal diffusivity dominates.

$$Pr = \frac{\mu c_p}{k} \tag{2.3}$$

Where μ is the dynamic viscosity of the fluid, c_p is the specific heat capacity at constant pressure, and k is the thermal conductivity of the fluid.

Reynolds number

The Reynolds number, Re, is the ratio of inertial forces to viscous forces. It is a helpful tool to determine the flow regime of a fluid. For low Reynolds numbers the fluid is dominated by viscous forces, and the flow is laminar, while for high Reynolds numbers, the fluid is likewise dominated by inertial forces, and the fluid is turbulent.

$$Re = \frac{VL}{\mu} \tag{2.4}$$

Where V is the fluid velocity, L is the characteristic length, and μ is the dynamic viscosity of the fluid.

2.2 Heat transfer parameters

2.2.1 The convection coefficient

Convective heat transfer is heat transfer that occurs between a fluid in motion and a surface when the two are at different temperatures. This heat transfer is sustained by both random molecular motion and the bulk motion of the fluid. This fluid motion is the key difference between convection and conduction, where conduction is heat transfer through direct contact with no movement involved [2].

With fluid-surface interaction, a velocity boundary layer will develop. Inside this boundary layer, the fluid velocity will gradually grow from zero at the surface to a velocity T_∞ associated with the flow. This is analogous to convective heat transfer, where a thermal boundary layer will develop if the surface and fluid are at two different temperatures. Fig. 2.1 illustrates the development of both the velocity and the thermal boundary layer.

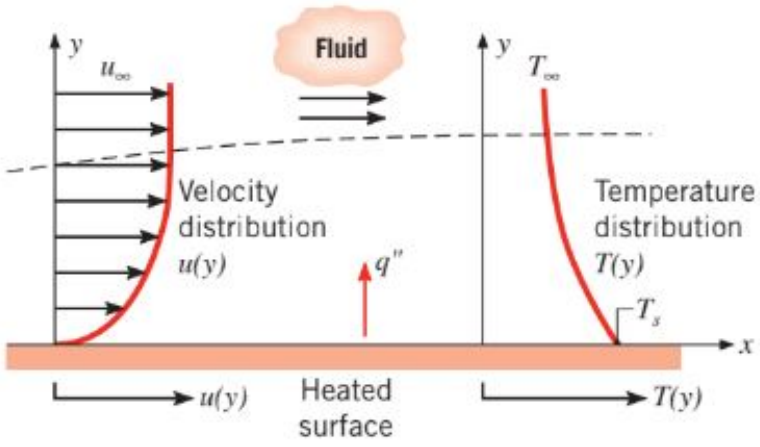

Figure 2.1: Boundary layer developments of a fluid flowing across a heated plate. Reproduced from [2].

The rate equation for convective heat transfer is known as *Newton's law of cooling*, and is expressed in (2.5).

$$q'' = h(T_S - T_\infty) \tag{2.5}$$

This equation shows that the convective heat flux, or heat transfer per unit area, q'', is proportional to the difference between T_S and T_∞, which is the surface temperature and fluid temperature, respectively. In the case where the flow has a higher temperature than the surface, i.e., $T_\infty > T_S$, the heat transfer will happen in the opposite direction, and it is common to write the temperature difference as $(T_\infty - T_S)$. The term h is the convection coefficient and is dependent on multiple fluid properties. The key to calculating conductive heat transfer is often determining this coefficient.

The convection coefficient is often expressed in terms of the dimensionless Nusselt number.

$$Nu \equiv \frac{hL}{k_f} \tag{2.6}$$

In many cases it is desirable to estimate the average convection coefficient to better calculate total heat transfer rate. This average convection coefficient is found by integrating the local convection coefficients over the entire surface:

$$\overline{h} = \frac{1}{A_s} \int h dA_s \tag{2.7}$$

It then follows that the total convection heat transfer rate may be expressed as:

$$q_{tot} = \overline{h} A_s (T_S - T_\infty) \tag{2.8}$$

This integration can however prove difficult for more complicated surfaces, but as with the local convection coefficient, it can be expressed by the average Nusselt number, $\overline{Nu}$. This average Nusselt number is in turn a function of both the Reynolds number, Re, and the Prandtl number, Pr, and can be expressed as:

$$\overline{Nu} \equiv \frac{\overline{h} L}{k_f} = f(Re, Pr) \tag{2.9}$$

Numerous empirical correlations of the average Nusselt number exist for a wide range of geometries. Among them is the *Gnielinski correlation*, which is for turbulent flow in tubes, and will be used in later calculations.

2.2.2 Thermal conductivity

Thermal conductivity, k, is a measure of a material's ability to conduct heat. It is a material specific property, and its values are often tabulated. For materials with low thermal conductivity, heat transfer will occur at a lower rate than in materials with high thermal conductivity. Conduction of heat happens as energy is transferred from more energetic particles to less energetic ones, i.e., from a high to a low temperature, as shown in Fig. 2.2. The corresponding rate equation is known as *Fourier's law* and is expressed in Eq. 2.10.

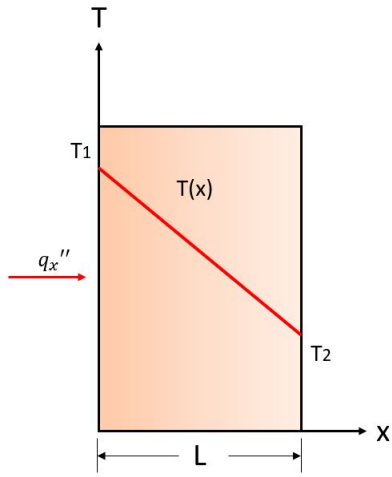

Figure 2.2: One-dimensional heat transfer by conduction.

$$q'' = k\frac{dT}{dx} = \frac{k}{L}(T_1 - T_2) \tag{2.10}$$

2.2.3 The overall heat transfer coefficient

The overall heat transfer coefficient, also referred to as the *U-value*, is a convenient tool when working with composite systems. It is, in essence, a merging of all the thermal conductivities and convection coefficients into one combined value. For an illustrative example of this, we can take the simple example from Fig. 2.5.

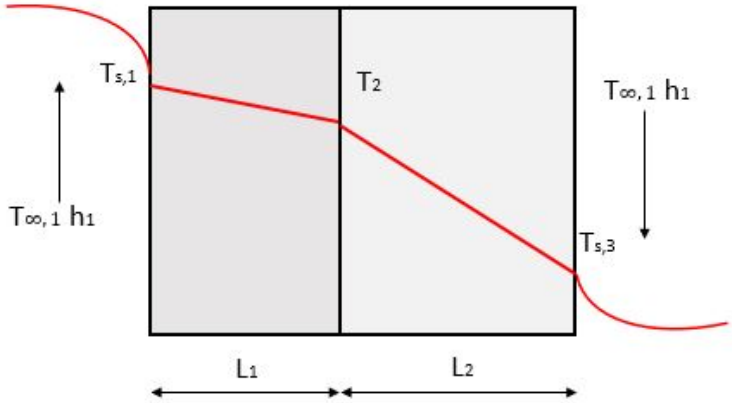

Figure 2.3: Heat transfer through composite wall.

The figure shows a composite wall with two materials of different width, L_1 and L_2, and with thermal conductivities k_1 and k_2, placed together between a hot fluid with temperature $T_{\infty,1}$, and a cold fluid with temperature $T_{\infty,3}$. This creates two surface temperatures, $T_{s,1}$ and $T_{s,3}$, and an intermediate temperature T_2 at the boundary between the two materials.

Using Newton's law of cooling and Fourier's law, we can set up the equation for the heat flux.

$$q''_x = h_1(T_{\infty,1} - T_{s,1}) = \frac{k_1}{L_1}(T_{s,1} - T_2) = \frac{k_2}{L_2}(T_2 - T_{s,3}) = h_2(T_{s,1} - T_{\infty,3}) \tag{2.11}$$

(2.11) can be rearranged to:

$$q''_x = \frac{T_{\infty,1} - T_{\infty,3}}{\frac{1}{h_1} + \frac{L_1}{k_1} + \frac{L_2}{k_2} + \frac{1}{h_2}} \tag{2.12}$$

where:

$$U = \left(\frac{1}{h_1} + \frac{L_1}{k_1} + \frac{L_2}{k_2} + \frac{1}{h_2} \right)^{-1} \tag{2.13}$$

The inverse of the U-value is called the thermal resistance, and is a measure of how well the material resists heat transfer.

For counter flow heat exchangers, the derivation is less trivial [2], but the general expression for the overall heat transfer coefficient is similar:

$$q = (UA)LMTD \tag{2.14}$$

Where A is the total heat transfer area, and $LMTD$ is the logarithmic mean temperature difference, defined as:

$$LMTD = \frac{(T_{1,in} - T_{2,out}) - (T_{1,out} - T_{2,in})}{ln\left(\frac{(T_{1,in} - T_{2,out})}{(T_{1,out} - T_{2,in})}\right)} \tag{2.15}$$

For radial systems, such as cylinders, the derivation of the overall heat transfer coefficient is similar to that of the composite wall, but with a key difference. The difference is that the temperature distribution associated with radial conduction is logarithmic, as opposed to linear, which it is for the plane wall [2]. This yields the following expression for a regular cylinder, based on the outside area:

$$U_o = \left(\frac{1}{h_o} + \frac{A_o}{2\pi kL} ln\frac{r_2}{r_1} + \frac{A_o}{A_i h_i} \right)^{-1} \tag{2.16}$$

where the subscripts i and o refer to the inner and outer surface of the cylinder, respectively.

2.3 Heat transfer enhancements

Looking at Eq. 2.8, we recognize that the only option for increasing the total heat transfer rate, provided that the temperature difference is not subject to change and the average convection coefficient is constant, is to increase the heat transfer area. Increasing the heat transfer area is achieved by adding extended surfaces, or fins, to the already existing surface. By doing this, the convection heat transfer is increased, and thereby the total heat transfer.

To evaluate the heat transfer to and from extended surfaces, one must first obtain the temperature distribution along the fin. This is important as the temperature is not constant along the surface of the fin, which means that the temperature difference between the surface and the surrounding fluid will not be constant either.

To simplify the evaluation, one must first make several assumptions. Firstly one-dimensional conditions are assumed in the longitudinal direction for straight fins, and in the radial direction for annular fins. This means that the temperature is only a function of either x or r. Steady-state conditions, constant thermal conductivity, negligible surface radiation, no heat generation, and uniform convection coefficient are also assumed [2].

The general form of the resulting energy equation is shown in Eq. 2.17, and the solution of which, combined with appropriate boundary conditions, provides the temperature distribution for extended surfaces.

$$\frac{d^2T}{dx^2} + \left(\frac{1}{A_c}\frac{dA_c}{dx}\right)\frac{dT}{dx} - \left(\frac{1}{A_c}\frac{h}{k}\frac{dA_s}{dx}\right)(T - T_\infty) = 0 \tag{2.17}$$

Here, A_s and A_c is the surface and cross-sectional area, respectively.

For a straight fin with a uniform cross-sectional area, 2.17 reduces to the linear, homogeneous, second order differential equation:

$$\frac{d^2T}{dx^2} - \frac{hP}{kA_c}(T - T_\infty) = 0 \tag{2.18}$$

where P is the fin perimeter.

For a solid, annular fin 2.17 becomes:

$$\frac{d^2T}{dr^2} + \frac{1}{r}\frac{dT}{dr} - \frac{2h}{kt}(T - T_\infty) = 0 \tag{2.19}$$

where t is the fin thickness. This equation is a modified Bessel equation of order zero, the general solution for which is shown below:

$$\theta(r) = C_1 I_0(mr) + C_2 K_0(mr) \tag{2.20}$$

where θ is the temperature difference $T - T_\infty$, and I_0 and K_0 are modified, zero-order Bessel functions. m is defined as:

$$m = \sqrt{2h/kt} \tag{2.21}$$

which can be recognized from the third term in 2.19.

Using Fourier's law of heat conduction 2.10 to express the fin heat transfer rate:

$$q_f = -kA\frac{dT}{dr} = -k2\pi rt\frac{d\theta}{dr} \tag{2.22}$$

While this is an example derivation, similar derivations can be done for a wide variety of geometries and fin types.

2.3.1 Fin efficiency

Fin efficiency is a very important tool for evaluating fin performance. Due to fins having a finite thermal conductivity, a thermal gradient will be formed along the fin, from the base to the tip. This temperature gradient means that the temperature difference, which is the driving force of convective heat transfer, will be lower along the fin. This will in turn result in a lower heat transfer compared to a fin with infinite conductance [1].

It is the ratio of these two heat transfer rates which defines the fin efficiency, η_f, as shown in 2.23.

$$\eta_f = \frac{q_f}{q_{max}} = \frac{q_f}{hA_f\theta_b} \tag{2.23}$$

Here, q_f is the fin heat transfer rate, and q_{max} is the hypothetical heat transfer rate where the fin has infinite conductance, and the entire fin is at the base temperature [2]. θ_b is the temperature difference between the base temperature and the surrounding fluid temperature. The convection coefficient, h, is assumed to be uniformly distributed over the fin area, A_f. This assumption is common, but not necessarily correct, and several corrections have been suggested [1].

Using the expression for fin heat transfer rate 2.22, we can derive the fin efficiency for a solid, annular fin by using the fin efficiency equation 2.23:

$$\eta_f = \frac{q_f}{h2\pi(r_2^2 - r_1^2)\theta_b} = \frac{2r_1}{m(r_2^2 - r_1^2)}\frac{K_1(mr_1)I_1(mr_2) - I_1(mr_1)K_1(mr_2)}{K_0(mr_1)I_1(mr_2) + I_0(mr_1)K_1(mr_2)} \tag{2.24}$$

As is the case for the derivation for q_f, the expression for fin efficiency can be obtained similarly for a wide range of geometries.

If the fin efficiency is taken into account, the *apparent* convection coefficient is not equal to the *actual* convection coefficient. The apparent convection coefficient is often the coefficient one would get directly from measurements, i.e., without factoring in the fins and fin efficiency, while the actual coefficient is the coefficient one would get if we *do* take the fins into account. To better illustrate this, we define the apparent convection coefficient as:

$$h_{app} = h_{conv}\left(\frac{A_{bt} + \eta_f A_f}{A_{tot}}\right) \tag{2.25}$$

Here, A_{bt} is the bare tube area, i.e. the tube area *not* covered by fins, and A_f is the finned area. A_{tot} is the total outside surface area, $A_{bt} + A_f$.

As the expression shows, h_{app} and h_{conv} will be equal if the fin efficiency is 1. This is not realistic, however, and therefore the apparent convection coefficient would be lower than the actual one.

The same correction must be made for equation 2.16 as well, where it is important to recognize that the outside convection coefficient is an *apparent* one, not an *actual* one. Rearranging the equation leaves us with the following expression for the apparent convection coefficient:

$$h_{app} = \left[A_o \left(\frac{1}{UA_o} - \frac{ln(r_2/r_1)}{2\pi kL} - \frac{1}{h_i A_i} \right) \right]^{-1} \tag{2.26}$$

By using these two expressions for the apparent convection coefficient, along with an appropriate expression for the fin efficiency, one can solve for the actual convection coefficient through an iterative procedure.

2.3.2 Fin types

For tube banks, extending the surface area would mean the addition of fins to the tubes.

There are three main methods of attaching fins to a tube, extruding, grooving, and welding. Extruding means creating the fins from the tube material itself, and has the benefit of having a perfect thermal contact between the tube and fins. The drawback of extruding fins is that the tube material needs to be soft, and it is, therefore, unsuited for use in high-temperature environments. Grooved fins are fins placed in grooves or serrations in the tube, which often causes imperfect thermal contacts and mechanical weakness. The last method, welding, is also the most suited for use at high temperatures. It has a better thermal connection and mechanical strength than grooved fins, and also a higher structural rigidity than extruded fins [1].

Increasing the average convection coefficient can be achieved through thinning of the boundary layers [9]. This relationship can be seen in equation 2.9, where a reduction of the boundary layer thickness will lead to an increase in the average convection coefficient. This thinning can be achieved by breaking the flow, creating more, small boundary layers.

Serrated fins have the advantage of both having an increased surface area compared to bare tubes, while also having more flow disruption, and therefore thinner boundary layers, than plain fins. Due to this fact, serrated fins are often used in industrial applications.

2.4 Tube vibration

This section contains an overview of essential tube parameters that need to be considered when calculating tube vibration. It also includes a condensed version of a previous literature search, with an emphasis on the forced vibration part of the vibration response prediction program. Lastly, it contains the theoretical basis of the free vibration part of the same program.

2.4.1 Tube parameters

Tube array configurations

The rows of a tube bank can be either be in-line, also referred to as aligned, or staggered in the direction of the fluid velocity. In an in-line array, the minimum flow area is at a constant location, while a staggered array has alternating placements of this minimum flow area.

The configuration is also characterized by parameters such as the transverse pitch, P_t, the longitudinal pitch, P_l, and the tube diameter, D, as well as the ratios between these. These definitions of these parameters can be viewed in Fig. 2.4 below.

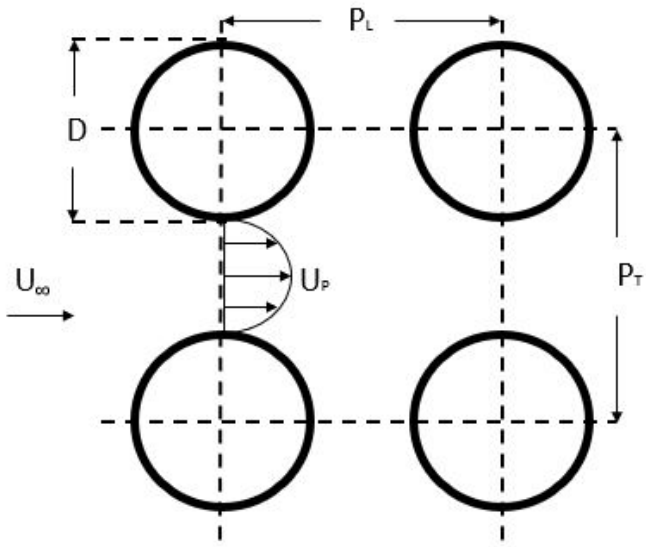

Figure 2.4: Illustrative graphic showing the definitions of transverse pitch, longitudinal pitch. Fluid path from left to right.

The hydraulic diameter

Due to the difference in behaviour of fluids around finned tubes, it is not applicable to use the bare tube diameter to estimate certain parameters. To counteract this, several different hydraulic tube diameters have been proposed.

A volumetrically based effective diameter has been proposed [10], and is on the form:

$$D_{vol} = \sqrt{(D_f^2 - D_b^2)\frac{t}{c} + D_b^2} \tag{2.27}$$

where D_f is the diameter from fin tip to fin tip, D_b is the bare tube diameter, t is the fin thickness and c is the fin pitch.

Mair et al. proposed an alternate variation of the effective diameter, based on the projected area of the finned tube [11]:

$$D_h = \frac{1}{c}[t(D_f - D_b) + cD_b] \tag{2.28}$$

As we can see, both versions of the effective diameter will reduce to the bare-tube diameter D_b when the fin width, t, is zero.

Lumsden and Weaver conclude that the hydraulic diameter, D_h, seems to be the most appropriate, especially for rotated square arrays, although there is a 4%-6% difference between the two [12].

It is also important to note that both these effective diameters were derived for plain finned tubes, i.e., not helically wound or serrated fins. The calculations would be much more complex and lengthier, especially for serrated fins. Despite this it has been shown by Mair [11] that the projected area based effective diameter is reasonably accurate in predicting vortex shedding, even for both helically wound and serrated fins.

Second moment of area

The second moment of area is a geometrical property of an area; in this case, the tube cross-section, which describes how points are distributed along the axis. The usual formula for an unfinned, circular tube's second moment of area is:

$$I = \frac{\pi}{64}(D_0^4 - D_i^4) \tag{2.29}$$

where D_o and D_i are the tube outside and inside diameters, respectively. For finned tubes, the equation must take into account the added area of the fins. For spiral-finned tubes the

expression, as found by Fischer [13], is:

$$\begin{aligned} I_{eff} &= I + \frac{\pi}{64}((D_0 + \frac{t_f}{2})^4 - D_0^4)F \\ F &= max\left[0; 1.0785666 \cdot \frac{t_f}{s_f} - 0.066319823\right] \end{aligned} \tag{2.30}$$

where t_f is the fin thickness, and s_f is the fin pitch. The parameter F was numerically obtained by Fischer [13] and curve-fitted by [14]. This correction for spiral-finned tubes is done due to the increased rigidity the fins will add to the tube. Had the fins not been helically wound, but welded in discrete rows or similar, the bending stiffness will not increase.

Mass per unit length

The equation for mass per unit length for finned tubes is:

$$m = \frac{\pi}{4}(\rho_t(D_o^2 - D_i^2) + \rho_i D_i^2 + \alpha\rho_o D_o^2) \tag{2.31}$$

where ρ_t is the tube material density, and ρ_i and ρ_o is the internal and external fluid density respectively. α, which can be neglected if the external fluid is a gas [13]. If either one of the fluid densities are two-phase, one must need to factor in the quality of the fluid in question to get an appropriate density. This can be done according to:

$$\rho_{i,o} = (1 - \epsilon_g)\rho_l + \epsilon_g\rho_g \tag{2.32}$$

where ϵ_g is the void fraction, and ρ_g and ρ_f are the density for gas- and fluid phase, respectively.

2.4.2 Vibration mechanisms

There are three main vibration mechanisms which can be dangerous and destructive in compact tube bundles, namely vortex shedding, fluid-elastic instability, and turbulent buffetting. All three mechanisms can contribute to excessive wear and tear on the materials, and ultimately may lead to premature destruction of the unit. It is therefore essential to understand the underlying theory behind each, to better design against them.

As the different vibration mechanisms that may occur in finned tube bundles were covered extensively through a literature search in the project thesis, this section will provide a summary of the main findings for each of the three vibration mechanisms.

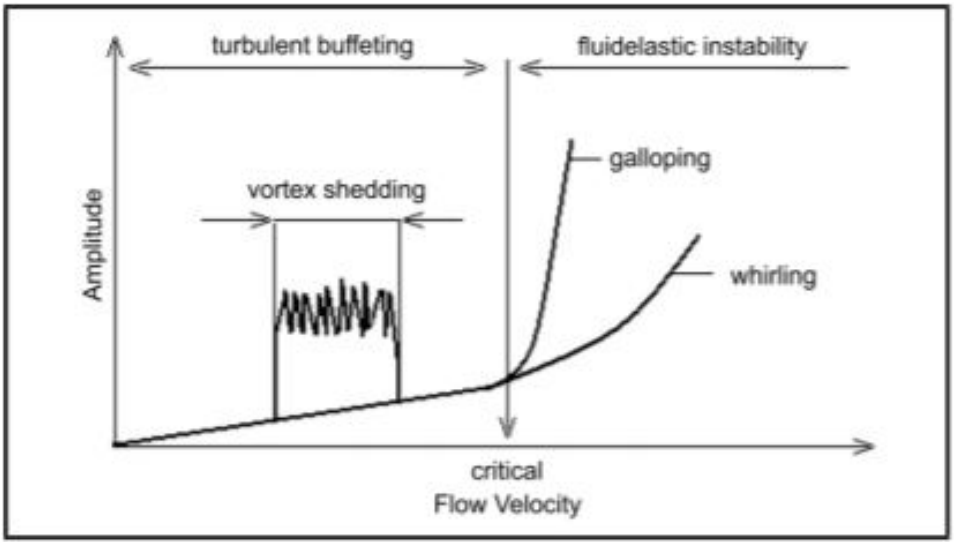

Figure 2.5: Illustrative graphic showing the three vibration mechanisms, vortex shedding fluidelastic instability and turbulent buffetting. Reproduced from [3].

Vortex shedding

Flow across a tube will generate a repeating pattern of vortices in the wake region, known as the Karman vortex street. This vortex street is characterized by periodic shedding of vortices on alternating sides of the tube surface. This shedding is dependent on the Reynolds number, and Fig. 2.6 shows how the flow around a cylinder evolves for certain ranges of Reynolds numbers.

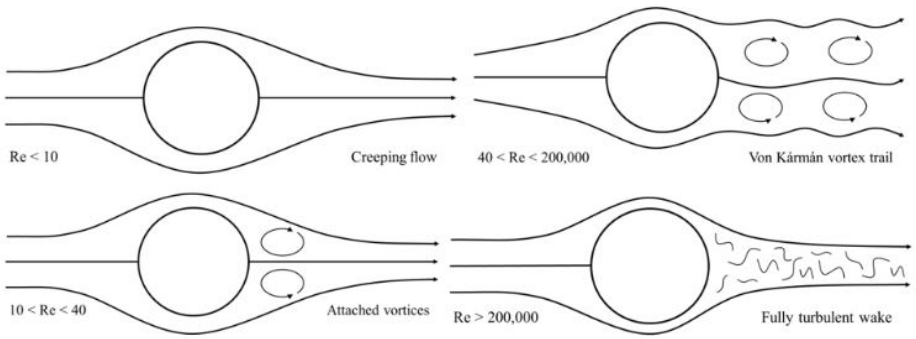

Figure 2.6: Vortice development for increasing Reynolds numbers. Reproduced from [4].

Experiments have shown that such periodic shedding occurs not only for isolated cylinders but also for each individual tube in tube banks. This periodic shedding can occur both in the transverse direction and parallel to the flow and will induce periodic pressure variations on the structure. In the transverse direction, these pressure variations will generate a transverse force, i.e., lift force, on the cylinder, and a drag force in the parallel direction. In the lift direction, the alternating force will have a dominant frequency called the vortex shedding frequency f_v. In the drag direction, the dominant frequency of the structure is twice the vortex shedding frequency [15]. This frequency is usually expressed by the dimensionless Strouhal number, St:

$$St = \frac{f_v D_h}{V} \tag{2.33}$$

where V is the flow velocity, f_v is the vortex shedding frequency, and D_h is the hydraulic diameter based on the projected area of finned tubes [16]. If the vortex shedding frequency is within $\pm 20\%$ of the natural tube frequency the vortex shedding may produce a significant tube vibration amplitude [17].

In tube bundles, expressions for the Strouhal numbers have to be found experimentally. They use the hydraulic diameter D_h as proposed by Mair [11], as his work has shown that it is applicable for finned tubes. To achieve this, they approximate expressions from experimental data sorted by bundle layout. The expressions are as follows:

$$St = \frac{1}{1.173} \frac{D_h}{P_t} \tag{2.34}$$

for normal triangular bundles,

$$St = \frac{1}{1.16} \frac{D_h}{P_t} \tag{2.35}$$

for rotated triangular bundles, and

$$St = \frac{1}{1.2} \frac{D_h}{P_t} \tag{2.36}$$

for square bundles. P_t is the transverse tube pitch, i.e., the shortest distance between two tube centers in the transverse direction. Similarly, P_l is the longitudinal tube pitch. A more detailed table of the dynamic lift coefficient and Strouhal numbers for these cases can be found in [18].

The previously mentioned lift force is expressed by Pettigrew et.al. (Pettigrew and gorman) as:

$$F_L(x) = C_L D \rho U_p(x)^2 / 2 \tag{2.37}$$

where C_L is an experimentally determined lift coefficient [18], D is the tube outside diameter, and U_p is the maximum pitch velocity. The lift coefficient is dependent on the pitch

ratio, and can be determined according to Eq. 2.38 [17].

$$\begin{aligned} C_L &= 0.075; P_t/d_h < 1.6 \\ C_L = 0.461\frac{P_t}{d_h} &- 0.663; 1.6 < P_t/d_h < 2.5 \\ C_L &= 0.49; P_t/d_h > 2.5 \end{aligned} \tag{2.38}$$

For a fully correlated lift force, i.e. when the vortices shed simultaneously across the length of the tube, and assuming that the damping is small, the general expression for the peak vibration amplitude at the *i*th mode can be expressed as:

$$Y(x) = \frac{\phi_i(x)}{m\pi^2 f_i^2 \delta} \int_0^l F_L(x')\phi_i(x')dx' \tag{2.39}$$

Where m is the mass per unit length, δ is the structural damping, $F_L(x')$ is the periodic shedding force along the tube, from Eq. 2.37 and ϕ_i is the normalized mode shape for the *i*th mode [18]. It is important to note that such a case is highly unlikely because the vortices will not necessarily shed simultaneously across the entire tube length. It is more likely that the shedding would occur more randomly. It is, however, a conservative choice to design for it, as it is the worst case scenario.

Singh & Soler [19] propose a simplified version for only the first mode of vibration, i.e., for one standing half wave, one a single span, where a uniform gas velocity and hinged support in both ends is assumed. In this case, the force F_L becomes constant, and the integral becomes simpler to evaluate. The maximum amplitude $Y(L/2)$ at mid-span becomes:

$$Y_{max} = \frac{F_L}{\pi^2 f_{n,1}^2 m\delta} \tag{2.40}$$

Pettigrew and Taylor suggest an acceptance criterion where the maximum root mean square tube vibration amplitude should be less than 2% of the outside tube diameter [20]:

$$Y_{max,r.m.s.} < 0.02D \tag{2.41}$$

Vortex shedding have been shown to also be existent in finned tube arrays. Ziada [16] found that for finned tubes, the vortex shedding frequency increases linearly with the velocity, just as for bare tubes. This frequency does, however, decrease following the addition of serrated fins. He also found that the frequency also decreases when you increase the fin density, which is supported by the findings of both Mair [11] and McClure & Yarusevych [21].

Fluid-elastic instability

Fluid-elastic instability is commonly characterized by several different mechanisms. B.W. Roberts created the first model attempting to analyze fluid-elastic instability in 1962 [22], which he dubbed "jet-switching". Jet-switching occurs when a fluid flows past a row of

tubes and forms discrete jets as it flows between tube pairs. These jets will create jet-pairings at the wake of the tube array, and can be switched back and forth if the tubes in a single row are displaced alternately up- and downstream by a sufficient amount, as can be seen in Fig. 2.7.

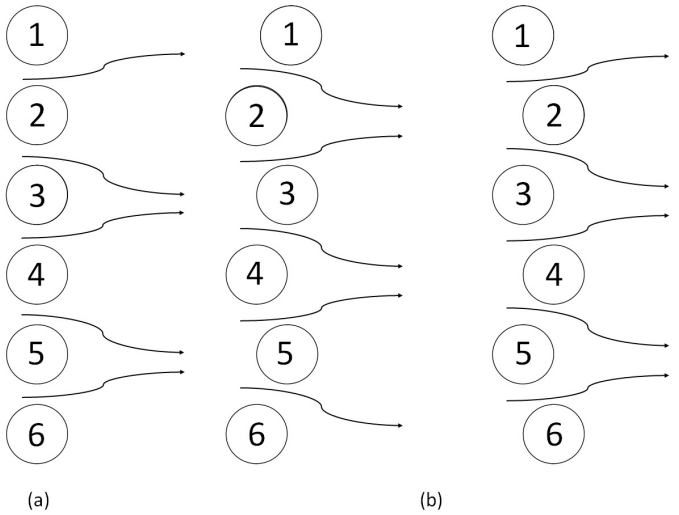

Figure 2.7: Jet pairing in the wake of a tube row. (a) Jet pairing in aligned row. (b) Jet switching caused by streamwise displacement of tubes.

These jets produce a pressure difference, which in turn produces a drag force obtained by integrating the pressure distribution around the cylinder circumference. The drag force on a tube increases dramatically if two jets are paired behind it, and decreases equally if two jets separate behind it [23]. This switching mechanism of increasing and decreasing drag force may cause detrimental tube vibration. Jet-switching cannot occur at all flow velocities, however, but only past a certain critical velocity. This critical velocity is expressed in its dimensionless form in the so-called "Connor's formula".

$$\frac{V_{cr}}{f_n D} = K(\frac{m\delta}{\rho D^2})^{\frac{1}{2}} \tag{2.42}$$

Here, the left hand side expressed the dimensionless critical pitch velocity, and the right hand side is the dimensionless mass damping parameter.

To minimize the risk of fluid-elastic instability the maximum flow velocity should be lower than the critical velocity as described in [24], i.e.

$$\frac{V_r}{V_{cr}} < 1 \tag{2.43}$$

Pettigrew and Taylor suggest an additional safety factor for further security, for example a ratio of 0.75 [20].
There have been few experiments on fluid-elastic instability for finned tunes. Lumsden [12], however, conducted experiments on two different tube geometries, in-line square and rotated square, where he found that V_{cr} increases for the in-line case, while it reduces for the rotated square case.

Turbulent buffetting

Turbulent buffeting, also called turbulence induced vibration or random excitation, is a vibration mechanism caused by random pressure fluctuations in the flow. This results in randomly forced oscillations in the tubes [25]. The nature of turbulent buffeting is highly complex, and because of this simulation and prediction of turbulent buffeting is very difficult. As a result of this, mostly empirical models have been utilized.

The cylinders are excited by these turbulent forces over a wide range of frequencies. This frequency range is, however, centered around a dominant frequency [15]. To better illustrate this phenomena, we can look to Weaver and Grover and their experimental results from 1977 [5], as shown in Fig. 2.8.

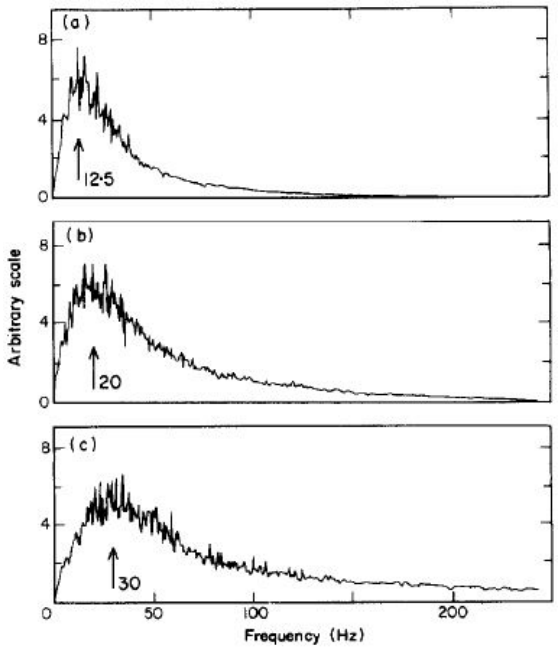

Figure 2.8: Turbulence velocity power spectra for (a) V=1.10 m/s, (b) V=2.32 m/s and (c) V=4.16 m/s. Reproduced from [5].

This dominant frequency can in turn be written in terms of the dimensionless Strouhal

number, as shown by Owen [26] in Eq. 2.44.

$$St_{tb} = \frac{f_{tb}D}{U}\frac{P_t P_l}{D^2} = [3.05(1 - \frac{D}{P_t})^2 + 0.28] \tag{2.44}$$

The tube response to turbulent buffeting must be calculated by random vibration theory, and summed over all significant vibration modes. The equation for the mean square response of the tubes is calculated by:

$$y^2(x) = \sum_{r=1}^{k}\sum_{s=1}^{k}\frac{\phi_r(x)\phi_s(x)}{16\pi^4 f_r^2 f_s^2}\int_0^\infty H_r(f)H_s(f)W(f)df \tag{2.45}$$

where, r and s is the mode number, k is the total number of modes considered, $H_{r,s}$ is the (complex) frequency response function defined as:

$$H_{r,s}(f) = [(1 - \frac{f^2}{f_{r,s}^2}) + j\frac{cf}{2\pi m f_{r,s}^2}]^{-1} \tag{2.46}$$

and W(f) is the weighting function defined below.

$$W(f) = \int_0^L \int_0^L R(x, x', f)\phi_r(x)\phi_s(x')dx\,dx' \tag{2.47}$$

Here, R(x,x',f) is the spatial correlation density function, which is an expression for the random force field. If it is assumed that the random force field is homogeneous and spatially correlated, i.e. independent of x, the spatial correlation density function can be expressed as R(x,x',f) = S(f), where S(f) is the power spectral density. The power spectral density is dependent on flow type, and the definitions of which can be found in [27].

Acoustic resonance

When the natural frequency of the structure is sufficiently close to the vortex shedding frequency, the two frequencies will synchronize [15]. This phenomenon is called lock-in. If this condition is met, combined with either sufficiently high acoustic energy or sufficiently low acoustic damping, the heat exchanger will experience acoustic resonance. This resonance will typically cause a very intense noise and may cause severe damage to both baffles and tubes. Acoustic resonance is a possible issue for heat exchangers with both finned and unfinned tubes [20].

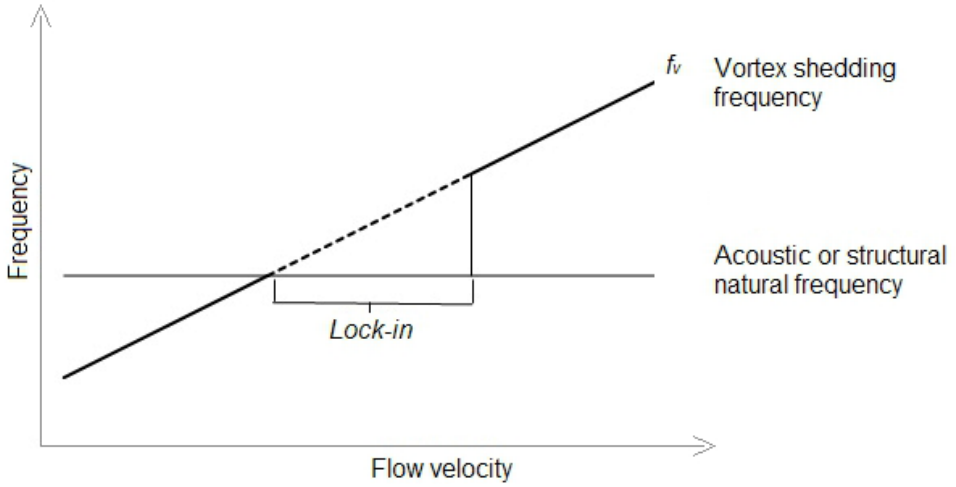

Figure 2.9: Lock-in conditions. Reproduced from [3].

The acoustic resonance frequencies of a duct containing a tube bundle can be defined using the effective speed of sound inside the heat exchanger, as well as the heat exchanger's physical dimensions [28]. This correction is made to adjust for the decrease in sound speed inside the heat exchanger [15].

$$f_a = \frac{nc_{eff}}{2W}; \qquad n = 1, 2, 3, ..., \infty \tag{2.48}$$

Where W is the heat exchanger dimension normal to the flow, and c_{eff} is the effective speed of sound, defined as [29]:

$$c_{eff} \approx c_0\sqrt{1+\sigma} \tag{2.49}$$

where σ is the fraction of the total volume occupied by pipes, and c_0 is the speed of sound, defined as [20]:

$$c_0 = \sqrt{\kappa p/\rho}; \qquad \kappa = c_p/c_v \tag{2.50}$$

where c_p and c_v are the specific heats at constant pressure and constant volume, respectively, p is the static pressure, and ρ is the air density.

According to Pettigrew & Taylor [20], the range of Strouhal numbers for which lock-in may be possible is $0.8St < St < 1.35St$. Blevins & Bressler [24] use a more conservative approach, where they suggest the range $0.6St < St < 1.48St$.

2.4.3 Natural frequencies and mode shapes

The natural frequencies and mode shapes of heat exchanger tubes are important to be aware of when designing against excessive vibration. This section will provide background for the calculation of these, both for single- and multi-span tubes.

Natural frequencies

Any flexible structures, including heat exchanger tubes, have infinite numbers of natural frequencies. These natural frequencies correspond to the frequencies at which the tube or structure vibrates when released from a non-equilibrium initial condition. If there is no damping present on the tubes, the tube motion will be sinusoidal in time, or the sum of different sine waves if several, higher natural frequencies are excited. The correlation between the natural frequencies and the sinusoidal waves is that each sine wave frequency is equal to a corresponding natural frequency. The motion of the tube can be written in the general form:

$$y(x,t) = \psi(x)sin(\omega t + \theta) \tag{2.51}$$

where $\psi(x)$ is the mode shape, which be discussed later, θ is the phase angle, and ω is the natural frequency [19]. To account for the infinite amount of both natural frequencies and mode shapes, the equation can be written as:

$$y(x,t) = \psi_n(x)sin(\omega_n t + \theta_n); \quad n = 1, 2, 3, ...\infty \tag{2.52}$$

The basic equation for the natural frequencies of a vibrating tube is:

$$f_n = \frac{\beta_n}{L^2}\left(\frac{EI}{m}\right)^{0.5} \tag{2.53}$$

where $\omega_n = 2\pi f_n$, m is the mass per unit length, and EI is the tube bending stiffness (also sometimes called flexural rigidity) and β_n is a dimensionless coefficient specific for each natural frequency. This dimensionless coefficient depends on tube end fixation and mode number. The bending stiffness is comprised of two elements, Young's modulus, E, and the tube's second moment of area, I. Young's modulus is a material-specific measure of the material's ability to withstand changes in length while under tensile or compressive stress.

Mode shapes

For each natural frequency, there is a corresponding mode shape. If a tube vibrates at only one natural frequency, the corresponding displacement, or amplitude, distribution is called the mode shape. They are somewhat similar to sine waves, but generally not exactly. If several natural frequencies are excited simultaneously, the mode shape is the sum of

the corresponding mode shapes. The mode shapes are generally defined arbitrarily and are often scaled according to a reference value, usually 1. This can be achieved by first finding the peak amplitude of the mode shape and then dividing all values by this, thereby making all the values in the range of ± 1. It can also be scaled so that the integral of the mode shape squared is equal to a specific value, i.e.:

$$\frac{1}{L}\int_0^L \phi_n^2(x)dx = C \tag{2.54}$$

where C is a constant, $\phi_n(x)$ is the *n*th mode shape, and L is the characteristic length. It is also important to note that because of this scaling, the mode shape does not specify the displacement response of the tube. For this, one would need to know the excitation forces.

Single span tube

The governing equation for the vibration of a single tube with fixed supports at both ends is:

$$-EI\frac{\delta^4 y}{\delta x^4} = m_0\frac{\delta^2 y}{\delta t^2} \tag{2.55}$$

where E is the Young's modulus of the tube material, I is the second moment of area, and m_0 is the tube's mass per unit length [19]. By substituting equation 2.51 for y into equation 2.55 and dividing by the sine term throughout, the equation becomes:

$$\frac{d^4\psi_n}{\delta x^4} = \kappa^4\psi_n \tag{2.56}$$

where

$$\kappa^4 = \frac{\omega_n^2 m_0}{EI} \tag{2.57}$$

By doing this, it becomes clear from equation 2.56 that the mode shape can be expressed by a function whose fourth derivative is equal to the function itself, multiplied by a constant κ^4. Singh & Soler [19] expresses this solution as:

$$\begin{aligned}\psi_n(x) = A_n(cos(\kappa x) + cosh(\kappa x)) + B_n(cos(\kappa x) - cosh(\kappa x)) \\ +C_n(sin(\kappa x) + sinh(\kappa x)) + D_n(sin(\kappa x) - sinh(\kappa x))\end{aligned} \tag{2.58}$$

Where A_n, B_n, C_n and D_n are chosen to satisfy the tube's end conditions.

Multi-span tubes

A multi-span tube is a tube supported on multiple places along its length. For heat exchangers, the supports are baffle supports, which are thin sheets of metal that supports the

tubes. These supports serve to separate the tube into individual spans. This means that for N spans, there are N-1 intermediate supports and two end-supports. The length of each individual span may vary, but it is usual for the two end spans to have the same length, and the N-1 middle spans to have the same length.

This multi-span configuration is what complicates the free-vibration analysis, as the tube cannot be treated by a single, comprehensive analysis. Instead, each span must be examined individually, each with it's own set of equations. The spans are considered as separate beams with the origin at its left support. The solution for span *i* is then:

$$\begin{aligned}\psi_i = B_i(cos(\kappa x_i) - cosh(\kappa x_i)) + C_i(sin(\kappa x_i) + sinh(\kappa x_i)) \\ +D_i(sin(\kappa x_i) - sinh(\kappa x_i))\end{aligned} \tag{2.59}$$

where B_i, C_i and D_i are undetermined constants for span *i*. The equation for each span in a multi-span tube is similar to the equation for a single tube, but with one key difference, namely that there is no A_i term coinciding with the A_n term in equation 2.58. This is due to the fact that the deflection is zero at the origin of each span, as well as at the rightmost point of span N. As $cos(\kappa x_i) + cosh(\kappa x_i)$ will not be zero at either x = 0 or x = L, A_i must then be set to zero.

Accompanying the solution 3.34 are sets of boundary conditions for each intermediate support and the two end spans. This is to ensure continuity between spans so that the mode shape continues through each support, even though there are separate equations for each span. For the leftmost span:

$$\psi'(0) = 0 \tag{2.60}$$

This means that the slope of the span at the leftmost support is equal to zero. For the intermediate supports between span *i* and *i+1*, we have the following three equations:

$$\psi(l_i) = 0 \tag{2.61}$$

$$\frac{d^2\psi_i}{dx_i^2}|_{x_i=l_i} = \frac{d^2\psi_{i+1}}{dx_{i+1}^2}|_{x_{i+1}=0} \tag{2.62}$$

$$\frac{d\psi_i}{dx_i}|_{x_i=l_i} = \frac{d\psi_{i+1}}{dx_{i+1}}|_{x_{i+1}=0} \tag{2.63}$$

where l_i is the length of each span. What the first equation shows is that there is no transverse displacement of the tube at any of the N-1 intermediate supports. The second and third boundary conditions indicate continuity of bending moment and slope, respectively, at the intermediate support between span *i* and *i+1*. This simply means that the slope and moment are continuous through the support. The last two boundary conditions are for span N, and are stated below.

$$\psi_N(l_N) = \psi'_N(l_N) = 0 \tag{2.64}$$

While this may only seem as one equation, it is two separate equations entirely. They state that the transverse displacement and slope of the span is zero at the rightmost end of span N, l_N. Thus, there is a total of 3N linear algebraic equations, three at each of the N-1 intermediate supports, one at the leftmost span, and one at the rightmost, together with the 3N unknowns ($B_i, C_i, D_i; i = 1, 2, ...N$).

This set of homogeneous algebraic equations is then formulated as a matrix, where a non-trivial solution, i.e., $B_i, C_i, D_i \neq 0$, would require the matrix determinant to be zero. Discrete values of κ, which makes this determinant zero define the modes. The natural frequency corresponding to each mode can after that be solved through equation 2.57. Each mode shape can then be determined through equation 3.34, by plotting over the total tube length and using the previously unknown B_i, C_i and D_i corresponding to each span.

This logic serves as the theoretical basis for the first part of the Fortran program, which is designed to return the N first natural frequencies and N corresponding mode shapes for a multi-span tube with N total spans.

3 Methodology

This chapter will provide an overview of the experimental setup for the heat exchange experiment, as well as the data reduction procedure and uncertainty calculation. A similar experiment was conducted in the author's project thesis, so parts of 3.1 is reused and modified from this work. It will also give a summary of the logic behind the vibration response prediction, in addition to the input values used.

3.1 Heat transfer experiment

This section provides a summary of the experiment, from the experimental setup to an extensive presentation of the final data reduction procedure conducted for both the pressure drop- and heat transfer experiments. In addition to this, estimations of the uncertainty ranges for relevant parameters are calculated and presented.

3.1.1 Experimental Setup

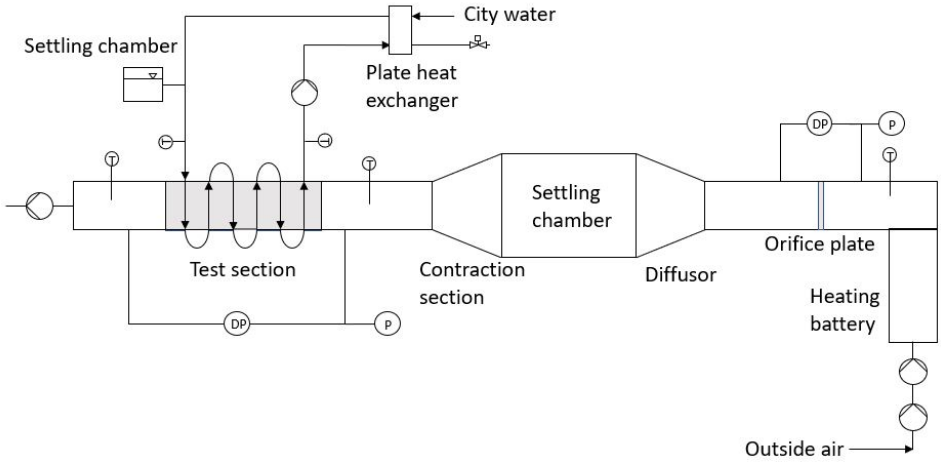

Figure 3.1: Flow diagram of experimental rig.

Fans and heating battery

Two fans and a heating battery was used to control the mass flow rate and temperature of the air. The fans were connected in series, and the fan speed was adjustable. This speed could be changed by as small increments as 1% of the maximum. There is also a third fan downstream of the test section, which serves the purpose of controlling the test section pressure. The heating battery is installed downstream of the two initial fans and has a power capacity of 400 kW. The air temperature could be adjusted either by directly setting a temperature, or by adjusting the power output of the heating battery.

Orifice

Two changeable orifice plates were used to help calculate the mass flow rate of air and subsequent Reynolds numbers. The details of how the orifices were used for these calculations are detailed later. These orifices were used for high and low flow rates, with orifice diameters of 221.86 and 139.90 mm, respectively.

Diffusor, settling chamber and contraction section

Downstream of the orifice, a section consisting of a diffusor, settling chamber and a contraction section is placed. The diffusor decreases the air velocity by enlarging the flow area, while also changing the shape of the flow area from a circular to a square geometry. The settling chamber serves the purpose of decreasing turbulence and creating a uniform flow distribution. This is vital to getting as accurate measurements as possible. The contraction section is designed for reducing the chamber dimensions to fit the test section.

Test section

The test section is the location where the heat transfer occurs. Warm air from the heating batteries is used as a substitute for flue gases, where the air transfers heat to the water circuit through finned tubes. The test section consists of two rectangular boxes with two tube rows each. The boxes each have a height of $H = 458$ mm, and a width of $W = 440$ mm. The tube bundles have a 30° layout, with a transverse pitch of $P_t = 26,5$ mm and a longitudinal pitch of $P_l = 60$ mm. The tube rows of each box both have 16 tubes in the first row, and 17 tubes in the second. This makes the total number of tubes 66, with 33 in each box.

The tubes themselves are elliptical, while the fins are solid, i.e., not serrated, and rectangular. The outer diameters of the tubes are 14 and 36 mm and inner diameters of 9 and 31 mm. This means that the wall thickness is 2,5 mm. The fins are 0,5 mm thick and have a height of 26 mm and a width of 55 mm. This geometry means that the spacing between fin tips, both in the transverse and longitudinal direction is 0,5 mm. Of the 440 mm length of each tube, the finned length is 420 mm, which means that there are unfinned portions of

each tube of 10 mm to either side. The fins are spaced 3,5 mm apart.

In Fig. 3.2a and Fig. 3.2b below, are illustrated cross sections of one of the two boxes of which the test section is comprised of and of a single tube, along with indicated dimensions for relevant parameters.

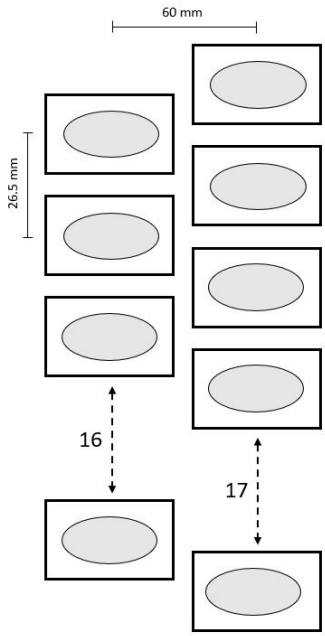

(a) Test section geometry.

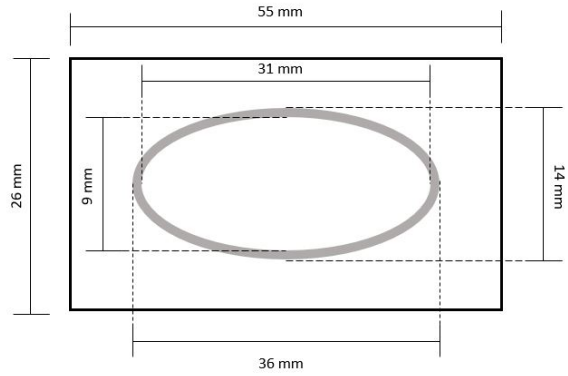

(b) Tube and fin geometry.

Water circuit

The water circuit is a closed circuit that had to be manually filled with water before performing the heat transfer measurements. The circulation of water was maintained using an adjustable speed pump. Using water as the cooling medium, unfortunately, increases the risk of corrosion in the tubes, which might influence the results, as corrosion adds more thermal resistance.

The heat removal was done by a plate heat exchanger, which transferred heat from the water circuit to the city water supply. The cold water supply was regulated by a manually operated valve to keep the water inlet temperature constant. The valve also had an automatic setting, but the manual option was chosen to secure stability.

3.1.2 Thermophysical properties

For all the calculations of temperature dependent thermophysical properties, the mean temperature, as defined in (3.1), has been used.

$$T = |\frac{T_{out} + T_{in}}{2}| \tag{3.1}$$

Air

The density calculation for air is done with the assumption of ideal gas, and a specific gas constant $R_s = 287.1 J/kgK$. The equation is as follows:

$$\rho_{air} = \frac{P_{t.s.} - \frac{1}{2}\Delta P_{t.s.}}{(T) \cdot R_s}; \qquad T[K] \tag{3.2}$$

In addition to the density, the specific heat capacity, $c_{p,air}$, and dynamic viscosity, μ_{air}, and thermal conductivity, k_{air}, are all temperature dependent. They must therefore be estimated numerically by (3.4) and (3.3), respectively.

$$\begin{aligned} c_{p,air} = R_s \cdot \left(B + (C-B) \cdot \left(\frac{T}{A+T}\right)^2\right) \cdot \left(1 - \frac{T}{A+T}\right. \\ \left. \cdot \left(D + E \cdot \frac{T}{A+T} + F \cdot \left(\frac{T}{A+T}\right)^2 + G \cdot \left(\frac{T}{A+T}\right)^3\right); \qquad T[K]\right. \end{aligned} \tag{3.3}$$

$$\mu_{air}, k_{air} = A + B \cdot T + C \cdot T^2 + D \cdot T^3 + E \cdot T^4; \qquad T[K] \tag{3.4}$$

The coefficients A to G are dependent on which parameter being calculated, and are tabulated in table 3.1 below.

Table 3.1: Thermophysical coefficients of air. Reproduced from [1].

	Thermal conductivity	**Dynamic viscosity**	**Specific heat capacity**
	k_{air} [W/mK]	μ_{air} [Pa· s]	$c_{p,air}$ [J/kgK]
A	$-0.908 \cdot 10^{-3}$	$-0.01702 \cdot 10^{-5}$	2548.9320
B	$0.112 \cdot 10^{-3}$	$0.79965 \cdot 10^{-7}$	3.5248
C	$-0.084333 \cdot 10^{-6}$	$-0.72183 \cdot 10^{-10}$	-0.6366
D	$0.05696 \cdot 10^{-9}$	$0.04960 \cdot 10^{-12}$	-3.4281
E	$-0.01563 \cdot 10^{-12}$	$-0.01388 \cdot 10^{-15}$	49.8238
F	-	-	-120.3466
G	-	-	98.8658

Water

The same procedure must be done for the thermophysical properties of water in the water circuit, with the addition of an equation for the water density, ρ_w. The coefficients are similarly tabulated in table 3.2.

$$\rho_w, k_w, c_{p,w} = A + B \cdot \frac{273.15}{T} + C \cdot \left(\frac{273.15}{T}\right)^2; \qquad T[K] \tag{3.5}$$

$$\mu_w = exp\left[A + B \cdot \frac{273.15}{T} + C \cdot \left(\frac{273.15}{T}\right)^2\right]; \qquad T[K] \tag{3.6}$$

Table 3.2: Thermophysical coefficients of water. Reproduced from [1].

	Thermal conductivity	**Dynamic viscosity**	**Specific heat capacity**	**Density**
	k_w [W/mK]	μ_w [Pa· s]	$c_{p,w}$ [J/kgK]	ρ_w [kg/m^3]
A	0.83818	-4.63024	5364.49	658.49825
B	-0.07629	-12.70106	-2590.01	664.71643
C	-0.20174	10.9899	1437.59	-322.61661

3.1.3 Uncertainty analysis

The uncertainties have been calculated by using the partial derivatives of the terms of each equation used. These partial derivatives are combined using Eq. 3.7.

$$\delta R = \sqrt{\sum_{n=1}^{N} \left(\frac{\delta R}{\delta X_n} \delta X_n\right)^2} \tag{3.7}$$

The confidence interval was chosen to be 95%, with the Student t multiplier 1.98, as suggested in (ISO 5167-1)[30]. The uncertainty intervals are based on the uncertainties for each measurement in the heat transfer measurments. All calculated uncertainties are presented as uncertainty intervals, along with an arithmetic mean uncertainty.

Mass flow rates

The uncertainty estimation for the air mass flow rate was done in accordance with (ISO 5167-1) [30]. The equation used is:

$$\frac{\delta \dot{m}_a}{\dot{m}_a} = \sqrt{\left(\frac{\delta C}{C}\right)^2 + \left(\frac{\delta \epsilon}{\epsilon}\right)^2 + \left(\frac{2\beta^4}{1-\beta^4}^2\right)^2 \cdot \left(\frac{\delta D}{D}+\right)^2} \\ \sqrt{+\left(\frac{2}{1-\beta^4}\right)^2 \cdot \left(\frac{\delta d}{d}\right)^2 + \frac{1}{4}\left(\frac{\delta \Delta P}{\Delta P}\right)^2 + \frac{1}{4}\left(\frac{\delta \rho_a}{\rho_a}\right)^2} \tag{3.8}$$

where β is the orifice to diameter ratio, ρ_a is the air density, Δp is the orifice pressure drop, D is the diameter and d is the orifice diameter. The partial derivatives of D, d, ϵ and C were calculated according to (ISO-1 5167). As ρ_a is a function of both the pressure and the temperature, it has to be calculated as follows:

$$\frac{\delta \rho_a}{\rho_a} = \sqrt{\left(\frac{\delta T}{T}\right)^2 + \left(\frac{\delta \Delta P}{\Delta P}\right)^2 + \left(\frac{\delta P}{P}\right)^2} \tag{3.9}$$

where T is the test section temperature, P is static pressure and ΔP is the test section pressure drop. For the water mass flow rate, the equation is:

$$\frac{\delta \dot{m}_w}{\dot{m}_w} = \sqrt{\left(\frac{\delta \rho_w}{\rho_w}\right)^2 + \left(\frac{\delta \dot{V}}{\dot{V}}\right)^2} \tag{3.10}$$

where ρ_w is the water density and $\dot{V}$ is the water volume flow rate, as measured in the experiments. The uncertainty ranges for air and water mass flows are presented in Table 3.3 below.

Table 3.3: Uncertainty ranges for mass flows.

Parameter	Symbol	Uncertainty range
Air mass flow	$\dot{m}_{air}$	$\pm(1.01-5.50\%)(\pm 3.26\%)$
Water mass flow	$\dot{m}_w$	$\pm(0.35-3.91\%)(\pm 1.40\%)$

Heat transfer rates

The uncertainties of the heat transfer rates, Q_{air} and Q_w, were calculated as presented in (3.11), and the calculated uncertainties are presented in Table 3.4 below.

$$\frac{\delta Q}{Q} = \sqrt{\left(\frac{\delta \dot{m}}{\dot{m}}\right)^2 + \left(\frac{\delta c_p}{c_p}\right)^2 + \left(\frac{\delta T}{T}\right)^2} \tag{3.11}$$

Here, $\dot{m}$, c_p and T are the respective mass flows, as calculated in (3.8) and (3.10), specific heat capacity and average temperature.

Table 3.4: Uncertainty ranges for heat transfer rates.

Parameter	Symbol	Uncertainty range
Heat transfer air	Q_{air}	$\pm(2.33 - 6.04\%)(\pm 4.18\%)$
Heat transfer water	Q_w	$\pm(0.39 - 6.72\%)(\pm 2.33\%)$

Pressure drop measurements

Table 3.5: Uncertainty ranges for Reynolds and Euler number for pressure drop measurements.

Parameter	Symbol	Corresponding equation	Uncertainty range
Reynolds number	Re_D	3.19	$\pm(3.39 - 6.80\%)(\pm 4.64\%)$
Euler number	Eu	3.20	$\pm(2.17 - 6.62\%)(\pm 3.90\%)$

Heat transfer measurements

Table 3.6: Uncertainty ranges for heat transfer parameters.

Parameter	Symbol	Corresponding equation	Uncertainty range
Water side convection coefficient	h_i	3.28	$\pm(2.65 - 2.69\%)(\pm 2.67\%)$
Log mean temperature difference	$LMTD$	2.15	$\pm(0.14 - 3.92\%)(\pm 1,34\%)$
Overall heat transfer coefficient	U	3.24	$\pm(1.03 - 6.82\%)(\pm 4.19\%)$
Air side convection coefficient	h_{air}	3.30	$\pm(4.67 - 8.22\%)(\pm 5.78\%)$
Air side Nusselt number	Nu	3.30	$\pm(4.67 - 8.22\%)(\pm 5.78\%)$

3.1.4 Measurements and data reduction procedures

The measurements were done in two sets of 8, one set for each of the two orifice plates. For the smallest orifice, the fan power was adjusted such that the pressure drop over the orifice was around 8000 Pa, which is the highest measurable value for the orifice pressure gauge. For the larger orifice, the pressure drop never reached this value, so the fan power was set to maximum output. The fan power was reduced by 10% after each measurement, to test for several different Reynolds numbers. As the heat transfer rate is proportional to the mass flow, it was necessary to reduce the heat battery power by the same amount to

maintain a relatively stable temperature difference inside the test section.

The measurements were automatically logged once every three seconds, and the total measuring time per fan power setting was around 15 minutes. This means that the total number of measurements per fan power setting was about 300. The measurements were then averaged to get as accurate values as possible, and a standard deviation was identified. These average values were the ones used in subsequent calculations.

Calculation of air mass flow rate

The data reduction procedure for calculating the air mass flow rate was adapted from (ISO-1 5167) [31], which is in turn used to find the Reynolds number, $Re_{D,t.s.}$ and the Euler number, Eu.

The equation for mass flow rate is as follows:

$$q_m = \frac{C}{\sqrt{1-\beta^4}} \epsilon \frac{\pi}{4} d^2 \sqrt{2\Delta p \rho} \tag{3.12}$$

where C is the discharge coefficient, and is in this case defined as:

$$\begin{aligned} C = 0.5961 + 0.0261\beta^2 - 0.216\beta^8 + 0.000521 \left(\frac{10^6\beta}{Re_D}\right)^{0.7} \\ + \left(0.0188 + 0.0063 \left(\frac{19000\beta}{Re_D}\right)^{0.8}\right) \beta^{3.5} \left(\frac{10^6}{Re_D}\right)^{0.3} \end{aligned} \tag{3.13}$$

and ϵ is the expansibility factor, defined below.

$$\epsilon = 1 - (0.351 + 0.256\beta^4 + 0.93\beta^8) \left[1 - \left(\frac{p_2}{p_1}\right)^{1/\kappa}\right] \tag{3.14}$$

In these equations, the factor β is the ratio of the orifice diameter, d, to the tube diameter, D, and p_1, p_2 and Δp is the upstream pressure, downstream pressure and pressure drop over the orifice, respectively. The pressure parameters are obtained from averaged samples in the test rig, and Δp is corrected for the baseline sample.

As both q_m are C dependent on the Reynolds number, an iterative computation is required to obtain q_m. The principle of this iterative solution is to first regroup all known values of 3.12 into one member, and the unknown values into the other. The known member is then the invariant, A, and is expressed as:

$$A = \frac{\epsilon d^2 \sqrt{2\Delta p \rho}}{\mu D \sqrt{1-\beta^4}} \tag{3.15}$$

where μ is the dynamic viscosity of the air. The iteration equation then becomes as shown below.

$$\frac{Re_D}{C} = A \tag{3.16}$$

The variable will then be Re_D, for which you first guess an initial value. This will, in turn, produce another value of Re_D by using equation 3.15. You then compare the two values, and if they are not equal, or within a specified limit, you repeat the procedure with your new Re_D. When your answer is satisfactory, the next step will then be to compute your mass flow rate, q_m, which can be computed as follows:

$$\dot{m} = \frac{\pi}{4}\mu D Re_D \tag{3.17}$$

When you have obtained the mass flow rate, you can compute the maximum velocity in for the test section. This maximum velocity, U_{max}, is the highest velocity the air can have inside the test section, and is defined as:

$$U_{max} = \frac{\dot{m}}{\rho F_{min}} \tag{3.18}$$

where F_{min} is the open area between the finned tubes in the test section. This velocity will enable you to compute both the test section Reynolds number, $Re_{D,t.s.}$, and the Euler number, Eu, as such:

$$Re_{D,t.s.} = \frac{\rho U_{max} D_h}{\mu} \tag{3.19}$$

$$Eu = \frac{\Delta P_{t.s.}}{\frac{1}{2} N_L \rho U_{max}^2} \tag{3.20}$$

Where, in Eq. 3.20, $\Delta P_{t.s.}$ is the pressure drop over the test section, obtained in the same manner as Δp in Eq. 3.12, and N_L is the number of tubes in the lateral direction. In Eq. 3.19, μ is the dynamic viscosity calculated as described in Eq. 3.4)

Heat transfer

After the data reduction procedure detailed in the previous subsection was finished and all air mass flow rates were calculated, the air-side convection coefficients could be found. The first step is to calculate the heat transferred *from* the air and *to* the water, respectively. Both heat transfers were calculated according to the heat transfer equation:

$$Q = \dot{m} c_p \Delta T \tag{3.21}$$

where Q is the heat duty, $\dot{m}$ is the mass flow, c_p is the specific heat capacity, and ΔT is the change in temperature.

For the air-side heat duty, Q_{air}, the mass flow was found by (3.17), and the resulting equation was as follows:

$$Q_{air} = \dot{m}_{air} c_{p,air} \Delta T_{air} \tag{3.22}$$

For the mass flow of water, the measured average volume flow, $\dot{V}_w$, was used for the calculation:

$$Q_w = \rho_w \dot{V}_w c_{p,w} \Delta T_w \tag{3.23}$$

Further, the U-value, U_{air}, was found by solving (3.24) for U_{air}:

$$Q_{air} = U_{air} A_{tot} LMTD \tag{3.24}$$

where $LMTD$ is the logarithmic temperature difference, defined below.

$$LMTD = \frac{(T_{a,i} - T_{w,o}) - (T_{a,o} - T_{w,i})}{ln\left((T_{a,i} - T_{w,o})/(T_{a,o} - T_{w,i})\right)} \tag{3.25}$$

The water side heat transfer coefficient, h_w, was found using the Gnielinski correlation [1] to find the Nusselt number, as shown in (3.26).

$$Nu_w = \frac{\frac{c_f}{2}(Re_w - 1000)Pr_w}{1 + 12.7\sqrt{\frac{c_f}{2}}(Pr_w^{2/3} - 1} \left(1 + (d_i/L)^{2/3}\right) \tag{3.26}$$

Where d_i and L is the tube inside diameter and tube length, respectively. Pr_w and Re_w are the Prandtl and Reynolds numbers, while $\frac{c_f}{2}$ is the fanning type friction coefficient defined below.

$$\frac{c_f}{2} = (2.236ln(Re_w) - 4.639)^{-2} \tag{3.27}$$

From the Nusselt number, h_w can be solved for.

$$h_w = \frac{k_w Nu_w}{d_i} \tag{3.28}$$

From these values it is now possible to solve for the average air side convection heat transfer coefficient, h_{air}. This is done by solving a set of equations through iteration by Microsoft Excel's function *Goal-seek*. Firstly, we define the apparent outside convection coefficient, h_{app} as in Eq. 3.30:

$$h_{app} = \left(\frac{1}{U_{air}} - A_{tot}\frac{ln(\frac{d_o}{d_i})}{2\pi k_w L} - \frac{A_{tot}}{A_i h_w}\right) \tag{3.29}$$

and, because we have a tube with serrated fins, this apparent convection coefficient will not be equal to the *actual* convection coefficient. We therefore again define h_{app} as in Eq. 2.26:

$$h_{app} = h_{conv}\left(\frac{A_{bt} + \eta_f A_f}{A_{tot}}\right) \tag{3.30}$$

where η_f is the fin efficiency. Due to the uncommon shape of the finned tubes, with elliptical tubes and rectangular fins, no general expression exists for the fin efficiency. Due to this, an empirical correlation must be used. This correlation was obtained from [14], and is as follows:

$$\eta_f = \frac{a + ch_{conv}}{1 + bh_{conv} + dh_{conv}^2}$$

$$\begin{aligned} a &= 0.999071685 \\ b &= 5,76561 \cdot 10^{-3} \\ c &= 1,343229 \cdot 10^{-3} \\ d &= 1,70017 \cdot 10^{-6} \end{aligned} \tag{3.31}$$

The iteration procedure involved finding a h_{conv} so that equations 3.29 and 3.30 becomes equal. After the air-side convection coefficients were established, Nusselt numbers could be calculated.

Through regression analysis, both Euler- and Nusselt dependencies on the Reynolds numbers were established. These were found by fitting the experimental data to equations 3.32 and 3.33, respectively. This is done to better compare the results to previous work.

$$Eu = C_1 Re_D^m \tag{3.32}$$

$$Nu = C_2 Re_D^n \tag{3.33}$$

In these equations, the constants C_1 and C_2 are geometry specific, and the exponents m and n are the main points of comparison with other work.

3.2 Vibration response prediction program

This section serves as an explanation of the vibration response prediction program, its logic, calculations, input, and output. The Fortran 90 code can be found in its entirety in Appendix A. The program can be divided into two main parts. The first part was programmed to calculate the N first natural frequencies and corresponding mode shapes for an N-span tube, with N-1 intermediate supports. The second part of the program checks the risks of forced vibration mechanisms. It calculates the vibration response of vortex shedding and turbulent buffetting and evaluates the danger of fluid-elastic instability and acoustic resonance. A 4-span tube is illustrated in Fig. 3.3 below. It serves as a visual representation of the tube used as an input in the vibration response prediction program.

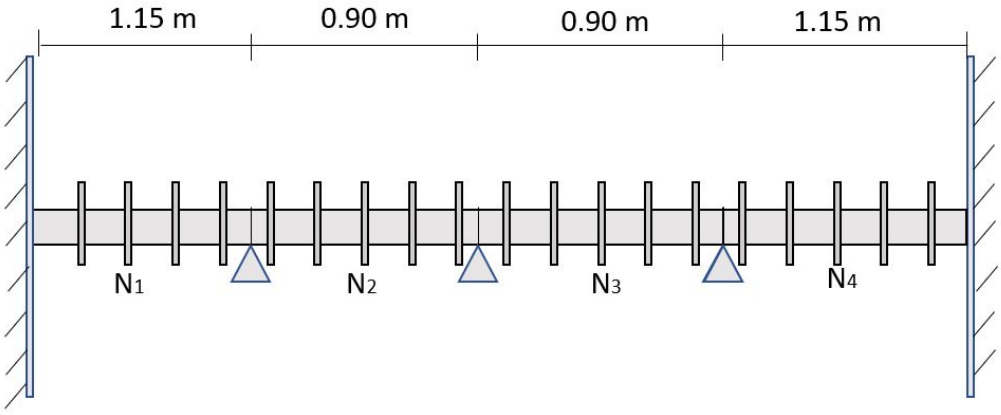

Figure 3.3: Illustration of tube used as input into vibration response prediction program.

3.2.1 Free vibration

The free vibration analysis was adapted from Singh & Solér's MULTSPAN program, which can be found in [19]. The program consists of two subroutines and one function, along with the main program. The input parameters are N, which is the total number of spans, the lengths of each respective span, VM, which is the mass per unit length of the tube, Ieff, which is the tube's second moment of area, as calculated in equation 2.30, and the Young's modulus of the tube material, in Pa.

The purpose of the main program, *Vibresponse* is to initialize several vectors, which are given values at later points in the program, along with calling up the other subroutines and functions. It also sets up a vector containing the individual lengths of each span, ELL. This vector then becomes a representation of the tube, with the first value being the

leftmost span and the Nth value being the rightmost span. The vectors used in the free vibration part are ELL, XKAPPA, FRENAT, B, C and D. ELL is the previously mentioned span-length vector, while the others are set to contain eigenvalues, natural frequencies, and the constants of integration B_i, C_i, and D_i, respectively. A vector X is also set up created, which later serves as a vector representation of the eigenvalue matrix.

The main program then calls the subroutine *natfre*, which first sets up an initial guess for the eigenvalue κ. This is done to reduce computing time [27]. After the initial guess is made, it is used as an input in the function *calc*. Calc then returns the determinant of the resulting matrix. This process is repeated, and the eigenvalue is recalculated several times if the determinant is non-zero. When the determinant eventually is sufficiently close to zero, then the eigenvalue is accepted and stored in the AKAP matrix for the calculation of the mode shape. The same is done with the natural frequency calculated from the eigenvalue.

The previously mentioned function, *calc*, serves the purpose of setting up the matrix with all the equations of motion, with the eigenvalue it is called up with. It then vectorizes the matrix by filling up the already initialized vector X and uses this as an input into the second subroutine, *minv*, which is short for *m*atrix *inv*erter. This subroutine inverts a vectorized matrix and returns the resulting determinant. *calc* then returns the determinant.

After all natural frequencies, eigenvalues and constants of integration are obtained, all the components for describing the mode shapes are available. In order to print out the mode shapes, each individual span is divided into 50 parts of equal length to get a representation that is as accurate as possible. This means that the step size for printing out the mode shape is 1/50th of the span length. By doing this, the mode shape can be represented according to equation 3.34, which is repeated below:

$$\begin{aligned}\psi_i = B_i(cos(\kappa_n x_i) - cosh(\kappa_n x_i)) + C_i(sin(\kappa_n x_i) + sinh(\kappa_n x_i)) \\ +D_i(sin(\kappa_n x_i) - sinh(\kappa_n x_i))\end{aligned} \tag{3.34}$$

where the equation expresses the transverse displacement at a point x_i. The subscripts n and i refers to the mode number in question and span number, respectively.

In Fig. 3.4 is a flowchart illustrating the program logic of the free vibration part of the vibration response prediction program.

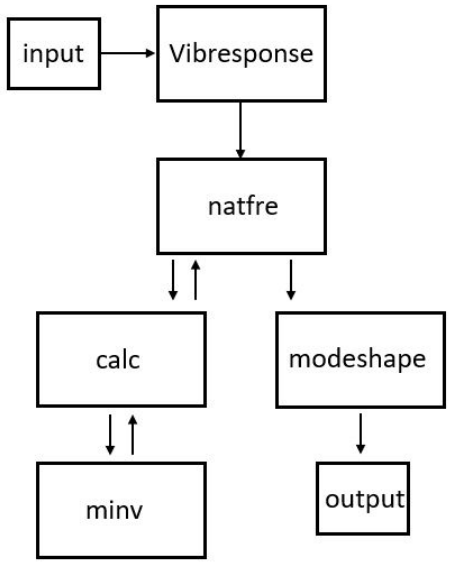

Figure 3.4: Program flowchart of for free vibration calculations.

3.2.2 Forced vibration

The underlying program logic for the forced vibration part of the vibration response prediction program was obtained from [27], while the theoretical background is summarized in the Theory chapter. It is, as previously mentioned, separated into four main parts. Vortex shedding, fluid-elastic instability, acoustic resonance, and turbulent buffetting. As it uses the mode shape and natural frequency of the tube, these calculations must be done after all the necessary mode shapes and natural frequencies are obtained.

The initial part of the vortex shedding amplitude prediction is the calculation of the periodic lift force along the tube, which is the cause of the vibration response. Firstly, a pitch-ratio dependent lift coefficient must be determined. Then, the lift force is calculated according to equation 2.37. If the number of tube spans is one, Eq. 2.40 is used to calculate the vibration response, and if the number of spans is two or more, Eq. 2.39 is used. A Strouhal number is then calculated as a function of the pitch ratio, and from this, a vortex shedding frequency is found through Eq. 2.33. The vortex shedding frequency is then checked to be within the critical range of the natural frequency of the tube, and a message of either "Danger of vortex shedding" or "No danger" is printed accordingly. This procedure is done for all the first N modes of vibration.

Regarding fluid-elastic instability, the critical velocity is first calculated according to Connor's formula, Eq. 2.42. After a critical velocity has been calculated, it is then compared

to the input fluid velocity. If the fluid velocity is larger than the critical one, a message of "Danger of instability is printed, and equivalently a message of "No danger" is printed if not. As with the vortex shedding calculation, this is done for all considered modes of vibration.

The turbulent buffetting calculation is the most complicated of all the forced vibration calculations. The function returns the RMS amplitude at a given location along the length axis of the tube. First, the real parts of the frequency response functions within Eq. 2.45 are calculated, which is then multiplied with the weighting function. After the terms inside the integral is established, it is then integrated through a ten point Gauss-Legendre scheme. When the integral is calculated, it is summed along with the rest of the terms over all significant modes of vibration. The same calculation is then repeated for all points along the tube, and the largest amplitude is returned.

Before the possibility of acoustic resonance can be estimated, several different parameters must be calculated. The total volume occupied by tubes and the following volume fraction are calculated and used to estimate the effective speed of sound inside the heat exchanger. This is then used in Eq. 2.48 to find the acoustic resonance frequency. To evaluate the danger of lock-in. this frequency is then compared to the vortex shedding frequency and all natural frequencies of the tube. A warning message is then printed if any of frequencies are within lock-in range.

3.2.3 Input parameters

Table 3.7 shows the parameters which were used as input variables in the vibration response prediction program. They were used both in the free and forced vibration parts. The parameters are related to tube geometry, tube composition, array configuration and the external fluid. In addition to this, in Table 3.8 are the initial calculations which were used at different parts of the program. The theoretical background for these calculations can be found in earlier chapters, and references to the specific equations used can also be found in the table.

Table 3.7: Input parameters for vibration response program.

Parameter	Symbol	Value	Unit
Tube inner diameter	D_i	10	[mm]
Tube outer diameter	D_o	12.38	[mm]
Young's modulus	E	193	[GPa]
Fin height	h_f	9.35	[mm]
Fin thickness	t_f	1.05	[mm]
Fin pitch	s_f	8.98	[mm]
Tube layout angle	-	30	[deg]
Tube bundle height	L_y	4.28	[m]
Transversal tube pitch	P_t	35.66	[mm]
Longitudinal tube pitch	P_l	32.57	[mm]
Support plate thickness	b	20	[mm]
Number of spans	N	4	[-]
Mid-span length	SPMID	0.9	[m]
End-span length	SPEND	1.15	[m]
Total tube length	L_{eff}	4.1	[m]
External fluid density	ρ_o	0.48	[kg/m^3]
Maximum fluid velocity	V_r	17	[m/s]

Table 3.8: Initial calculations of input parameters.

Parameter	Symbol	Value	Unit	Equation
Effective mass	m	1.411	[kg/m]	2.31
2nd moment of area	I_{eff}	6.75E-10	[m^4]	2.30
Total damping	δ	0.031	[-]	
Hydraulic diameter	d_h	14.6	[mm]	2.28

In order to best verify the results, these input values and initial calculations are the same ones used in the worked example found in [17]. The results from this worked example were used as the benchmark values for verification of the results from the vibration response prediction program. This does, however, only apply to the first natural frequency and the corresponding mode shape, as this was the only mode considered in Næss' work.

4 Results and discussion

4.1 Heat transfer experiment

In this section are presented the results from the pressure drop and heat transfer calculations. They are represented by Euler-Reynolds, Fig. 4.1, and Nusselt-Reynolds, Fig. 4.2, graphs. Each graph is accompanied by two equations, one representing the results from the measurements gathered by using the small orifice, and one for the large orifice. These equations were established through regression analysis, and the subscripts LO and SO represent the large and small orifice, respectively.

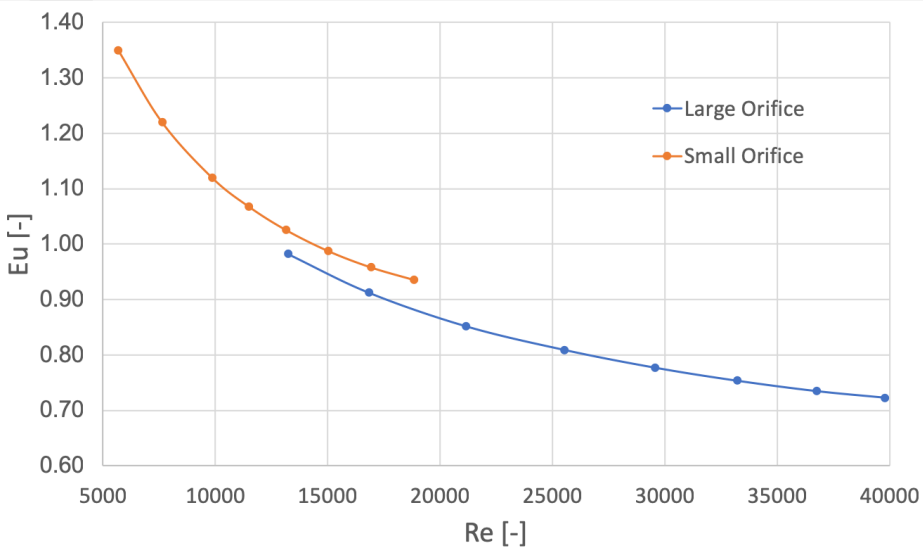

Figure 4.1: Euler-Reynolds correlations of pressure drop calculations.

$$\begin{aligned} Eu_{LO} &= 13.910 Re^{-0.28} \\ Eu_{SO} &= 19.129 Re^{-0.31} \end{aligned} \tag{4.1}$$

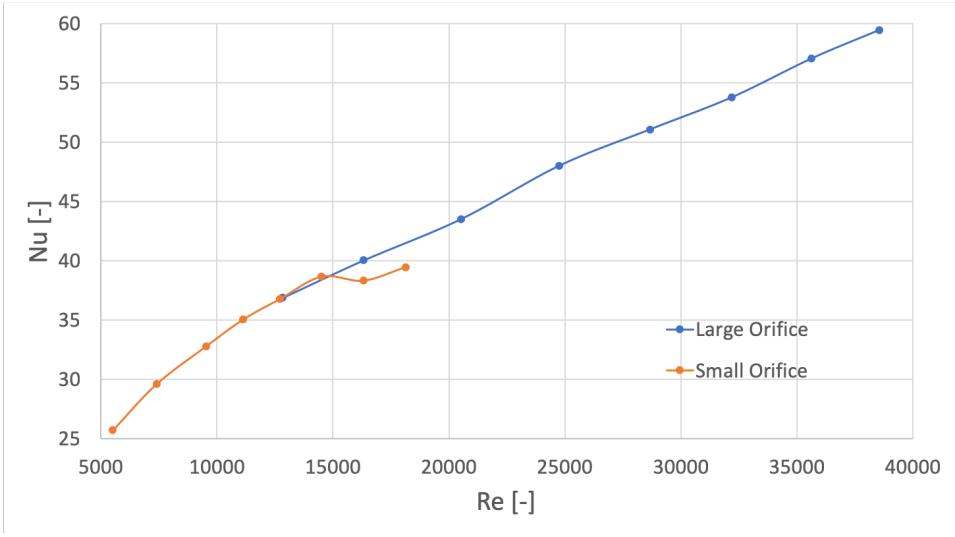

Figure 4.2: Nusselt-Reynolds correlations of heat transfer calculations.

$$\begin{aligned} Nu_{LO} &= 0.576 Re^{0.44} \\ Nu_{SO} &= 1.152 Re^{0.36} \end{aligned} \tag{4.2}$$

4.1.1 Comparison to published correlations

The basis of this comparison comes from the extensive literature review done by Holfeld [1], where the Reynolds number exponents for different comparable experiments are summarized in a thorough way. Correlations for both serrated-fin and and solid-fin tubes are presented in [1], but only those for solid-fin tubes will be considered in this section.

Pressure drop

As can be seen from Eq. 4.1 the Reynolds number exponents are -0.28 and -0.31 for the large and small orifice, respectively. Despite the disparity between the two lines, the exponents are very similar, with an arithmetic average of 0.295. This value is within the range of previous work [1]. This range is between -0.23 and -0.32 for similar experiments concerning pressure drop over finned tubes.

The implications of these results are that the pressure drop correlations are normal, despite the unusual geometry. While the geometry may have an effect, the correlations does not particularly stick out compared to previous work.

Heat transfer

The span of Reynolds number exponents in Nusselt number correlations are spread relatively evenly between 0.6 and 0.8 [1]. As previously mentioned, the corresponding exponents found in this experiment are 0.36 and 0.44 for the small and large orifice, respectively. If the average exponent of 0.4 is considered, it will be exactly half of the highest Reynolds number, and 2/3rd of the smallest. Also, if only the more reliable results from the large orifice is considered the exponent would still be 0.16 off the lowest value of the range. This shows that the exponents resulting from this experiment are far removed from comparable previous work.

While most other experiments have been done for circular tubes, Huang & Pu have done similar experiments with elliptical tubes, and use the correlation in Eq. 4.3 to express their results [32]. This method may be the most relevant for elliptical tubes, as the thermal-hydraulic behaviour would perhaps be different than for circular tubes.

$$Nu = CRe^{m}Pr^{0.38} \tag{4.3}$$

In this equation, Huang & Pu use an effective diameter for elliptical tubes defined in Eq. 4.4 as:

$$d_e = \frac{A_r d_r + A_f \sqrt{\frac{A_f}{2N}}}{A_r + A_f} \tag{4.4}$$

where A_r is the bare tube area, A_f is the fin area, N is the fin density. d_r is a geometrical parameter regarding elliptical tubes defined below.

$$d_r = \frac{ab}{\sqrt{\frac{a^2+b^2}{2}}} \tag{4.5}$$

Here, a and b is the long and short axis of the ellipse, respectively. They did experiments for several different ratios of a/b, where C_1 = 0.148, m = 0.632 for a ratio of 2.5. This is the ratio closest to that of this experiment where a/b = 2.57.

Using this correlation, the regression analysis yields C = 2.522, m = 0.363 for the small orifice, and C = 1.228, m = 0.4357 for the large orifice. These correlations show the same tendency as the previous, where the Nusselt number is significantly lower than comparable work. While it is difficult to ascertain exactly what the root cause of these discrepancies are, calculations were performed to investigate whether fouling may have been a factor. This theory will be investigated further on in this section.

4.1.2 Discussion

Euler number inconsistency

As Fig. 4.1 shows, the Euler numbers representing the two orifices do not overlap. This is again shown in their respective regression equations, Eq. 4.1, where both the constants

and the Reynolds number exponents differ. This is counterintuitive to the theory behind the calculations. As mentioned previously, the Euler number is a measure of the ratio of pressure to inertia. Therefore, because the test section geometry is constant, the pressure drop and subsequent Euler number corresponding to a certain Reynolds number should be constant as well. The graph does not support this, but instead shows a consistent difference between the Euler numbers for each of the orifices. In Table 4.1 are tabulated the Reynolds numbers with corresponding Euler numbers for the data points with overlapping Reynolds numbers, along with the percentage difference between the two measurement series (Δ).

Table 4.1: Deviation of Euler numbers for overlapping Reynolds numbers.

Re [-]	**Eu [-]**	**Δ [%]**
18 147	30.95	5.94
16 312	0.97	5.13
14 509	1.00	4.64
12 711	1.03	4.47

As Table 4.1 shows, the percentage differences between the Euler numbers are relatively similar but decreases along with the Reynolds number, which might still suggest a dependency on the Reynolds number. This may indicate that the source of the error lies in the calculation of the air mass flow rate. Whether this error lies in the calculations in the data reduction procedure from (ISO 5167) [30] or in any other calculations regarding the mass flow rate is uncertain and would need further investigation. This is supported by the relatively low average uncertainty of the air mass flow ($\pm$3.26 %) and Reynolds number ($\pm$ 4.64 %), which shows that this error may be systematic rather than random.

Nusselt number inconsistency

As Fig. 4.2 clearly shows, there are two measurement points that both stand out compared to the other measurements. These points correspond to Reynolds numbers of 16 312 and 18 147, with corresponding Nusselt numbers of 38.33 and 39.35, respectively. These points prevent the two lines representing the correlations for the small and large orifices to overlap, as had been the tendency of the other overlapping data points. These inconsistencies have been emphasized in Fig. 4.3 below, which is a magnified version of Fig. 4.2 in which the two data points are emphasized with a red rectangle.

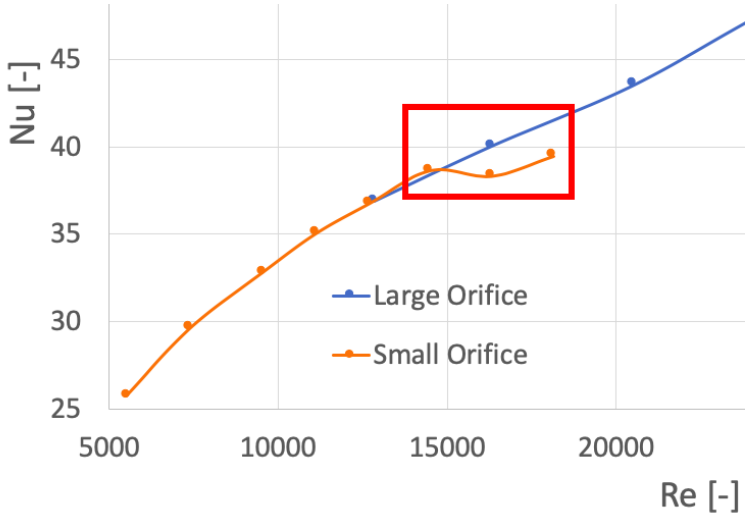

Figure 4.3: Nusselt-Reynolds correlations of heat transfer calculations.

These two Nusselt numbers represent deviations of 6.76 % and 8.66 % from the trend line representing the large orifice. This was calculated by inserting their Reynolds numbers into the regression analysis equation for the large orifice and calculating the percentage deviation of the two values. Comparatively, the closest other data point to these two, corresponding to respective Reynolds- and Nusselt numbers of 14 509 and 38.66, deviates only by 0.97 %. In Table 4.2 below are tabulated all the Reynolds numbers from the measurements with the small orifice, their corresponding Nusselt numbers, along with their percentage deviation (Δ). As the table clearly shows, the two values deviate by more than the others. This further emphasizes the possibility that some error in the measurements has occurred.

Table 4.2: Deviation of small orifice Nusselt numbers from large orifice.

Re [-]	**Nu [-]**	**Δ [%]**
18 147	39.47	8.30
16 312	38.33	6.77
14 509	38.66	0.98
12 711	36.77	0.17
11 129	35.05	-0.88
9 539	32.80	-1.04
7 395	29.61	-2.01
5 516	25.72	-0.84

This error may have come as a result of an issue with the water-side pump, which regulated the water volume flow. This issue lead to different pump speeds for the two previously

mentioned measurements, compared to the previous ones. As all calculations were done similarly and with no other noticeable differences, this seems the likely culprit. A more thorough investigation is needed, however, to conclude anything for certain.

Fouling factor estimation

Stagnant water at elevated temperatures will in many cases cause the metal tubes to rust on the inside. As this has been the case for the tubes used in this experiment, there is a cause for concern that there may be a layer of rust present. Such a layer will serve as an added thermal resistance, and will then increase the total resistance. The fouling is usually presented as a fouling factor, R_f. To account for this fouling factor, a small modification must be done to Eq. 2.26. The modified equation, where the fouling factor is added as a thermal resistance is shown below.

$$h_{app} = \left[A_o \left(\frac{1}{UA_o} - \frac{ln(r_2/r_1)}{2\pi kL} - \frac{1}{h_i A_i} - \frac{1}{R_f A_i} \right) \right]^{-1} \tag{4.6}$$

In an attempt to estimate R_f, the iteration procedure for estimating the convection heat transfer coefficient was re-done with different fouling factors. This procedure was repeated until the exponent of the Reynolds number in the Nusselt number expression for the large orifice was beyond the previously mentioned range of 0.6-0.8 from comparable previous work. In Table 4.3 are tabulated values of the fouling factor with the resulting exponent value for the large orifice, as well as the respective change from the original value. This was also recalculated with Eq. 4.3, to compare the results to those of similar geometry.

Table 4.3: Changes in Reynolds number exponents for different fouling factor estimations. Calculated by Eq. 3.33 and Eq. 4.3

Fouling factor [m^2K/W]	**Exponent [-] Eq. 3.33**	Δ	**Exponent [-] Eq. 4.3**	Δ
0.0000	0.44	0	0.44	0
0.0001	0.47	0.03	0.47	0
0.0002	0.51	0.07	0.51	0.07
0.0003	0.55	0.11	0.55	0.11
0.0004	0.61	0.17	0.60	0.16
0.0005	0.67	0.23	0.66	0.23
0.0006	0.74	0.30	0.74	0.30
0.0007	0.83	0.39	0.83	0.39

As can be seen in the table, the exponents resulting from both Eq. 3.33 and Eq. 4.3 are highly similar, with the only exception being a difference of 0.01 for R_f = 0.0004 and 0.0005 m^2K/W. By reviewing the results, it can be seen that this added fouling factor of R_f = 0.0004 m^2K/W resulted in a Reynolds number exponents of 0.61 and 0.6, which

makes it within the range of previous work. The Reynolds number exponent of 0.6, when using Eq. 4.3 is also similar to that of Huang & Pu, which is 0.632. This shows that a fouling factor of around 0.0004 may be the most accurate, as Huang & Pu utilized a similar geometry to that of this experiment. This value is higher than the 0.0001-0.0002 range of representative fouling factors for water given in *Fundamentals of Heat and Mass Transfer* [2], but is still of comparable size. While it would be hasty to assume that this theoretical fouling factor was the cause of the discrepancy between the results from this thesis and that of previous work, it shows that an added fouling factor within a reasonable limit would correlate these results nicely to the ones from previous experiments [1].

4.2 Vibration response prediction

4.2.1 Free vibration

This section will provide a summary of the results regarding the free vibration part of the vibration response prediction program. The first four natural frequencies of the heat exchanger tube can be found in Table 4.4, while the mode shapes corresponding to each natural frequencies are displayed in Fig. 4.4a, 4.4b, 4.4c and 4.4d.

Table 4.4: First four natural frequencies of heat exchanger tube.

$f_{n,1}$	18.176 Hz
$f_{n,2}$	20.518 Hz
$f_{n,3}$	27.471 Hz
$f_{n,4}$	36.335 Hz

As the figures show, all mode shapes have clearly defined peaks at the middle of each respective span, which fits the theory as explained earlier. In addition to this, all modes shapes are zero at the supports, i.e. between the spans. With this, it can be assumed that all end conditions are implemented correctly. The mode shapes are normalized according to their largest displacements, so that the maximum absolute value of each mode shape is 1.

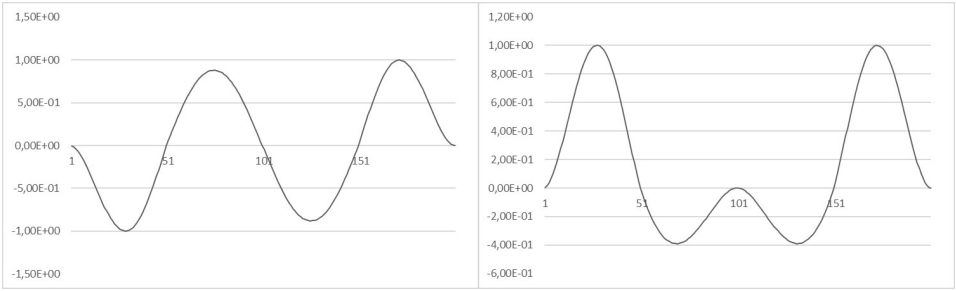

(a) First mode. **(b)** Second mode.

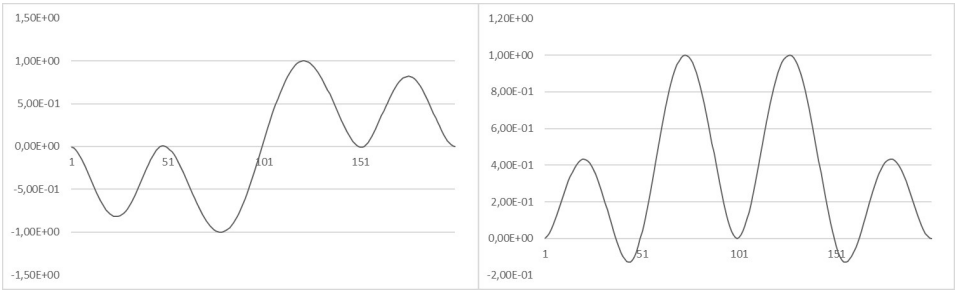

(c) Third mode. **(d)** Fourth mode.

4.2.2 Forced vibration

This section will present the output from the forced vibration part of the vibration response prediction program. The results are divided into subsections, where each subsection will focus on one of the four forced vibration mechanisms that are covered in this thesis, namely vortex shedding, fluid-elastic instability, acoustic resonance and turbulent buffetting. This section is concluded with a comparison of these results and the previously mentioned calculations done by Næss [17].

Vortex shedding

Table 4.5: Results from vortex shedding analysis.

Parameter	Value	Units	Eq.
St	0.237	[-]	2.34
f_{vs}	276	Hz	2.33
F_L	0.469	N/m	2.37
C_L	0.463	[-]	[-]
Y_{max}	5.49	mm	2.39

As Table 4.5 shows, the vortex shedding frequency is much larger than any of the natural frequencies calculated by the free vibration analysis, as can be seen in Table 4.4. This means that the vortex shedding frequency is safely outside the ± 20 % of the natural frequency required for any sort of significant amplitude to occur. Because of this, the maximum amplitude given in the table is not strictly accurate, but serves as a good indication of a possible amplitude regardless.

Fluid-elastic instability

To minimize the risk of fluid-elastic instability the critical velocity should be lower than the maximum fluid velocity, as stated in Eq. 2.43. The program first calculates the critical velocity for each natural frequency, and then checks the ratio of the maximum velocity to the critical velocity. The results of these calculations are presented in Table 4.6 below.

Table 4.6: Critical velocities and velocity ratios of the first four modes. All velocities are in [m/s].

	V_{cr}	V_r/V_{cr}
Mode 1	18.11	0.94
Mode 2	20.44	0.83
Mode 3	27.37	0.62
Mode 4	36.20	0.47

As the table above shows, neither of the ratios of maximum velocity to critical velocity are within the critical range.

Acoustic resonance

To check for acoustic resonance, an acoustic resonance frequency, f_a was calculated from Eq. 2.48. The ratio of the acoustic resonance frequency to the vortex shedding frequency was then calculated to ascertain whether lock-in may be an issue. Lastly, the ratios of the acoustic resonance frequency to the first four natural frequencies wwew found. These data are presented in Table 4.7.

Table 4.7: Acoustic resonance frequency and frequency ratios.

$f_{a,1}$	49.40 [Hz]
f_a/f_{vs}	0.18
$f_a/f_{n,1}$	2.74
$f_a/f_{n,2}$	2.42
$f_a/f_{n,3}$	1.81
$f_a/f_{n,4}$	1.37

The results show that f_a/f_{vs} is safely outside the previously established lock-in range of $0.8 < f_a/f_{vs}1,35$. Despite this, the ratio of the acoustic resonance frequency to the fourth

natural frequency is within the more conservative range suggested by Blevins & Bressler [24]. The ratios of acoustic resonance frequency to natural frequency are all safely outside the ± 20 % range where excessive vibration may occur.

Turbulent buffetting

The resulting maximum RMS amplitude caused by turbulent buffetting was calculated to be 0.005 mm. This is less then the allowable 2 % of the tube outside diameter, as suggested by Pettigrew & Taylor [18].

4.2.3 Benchmarking

The results from the vibration analysis were benchmarked against a previous worked example by Næss, in order to verify the results. The worked example can be found in its entirety in the appendix of [17]. After this benchmarking was done, and the results were found to be satisfactory, expansions of the program could be made. This section will provide a comparison between the results from the original worked example and the results from the vibration analysis program, which can be seen in Table 4.8. It is important to note that Næss' calculations are for the first mode of vibration only. Because of this, only the results based on the first mode of vibration and first natural frequencies will be considered and compared.

Table 4.8: Results from vortex shedding analysis.

Parameter	Output	Næss	% Diff.
$f_{n,1}$	18.176 [Hz]	17.81 [Hz]	+2.06%.
V_{cr}	18.11 [m/s]	17.74* [m/s]	+2.08%
F_L	0.469 [N/m]	0.47 [N/m]	0.0%
C_L	0.463 [-]	0.466 [-]	-0.64%
St	0.237 [-]	0.278 [-]	-14.74%
f_{vs}	275.56 [Hz]	324.68 [Hz]	+15.12%
f_a	49.36 [Hz]	51.60 [Hz]	-4.34%
Y_{rms}	0.005 [mm]	0.005 [mm]	0.0%

*In Næss' paper this value is listed as 23.31 m/s. This value has since been found to be erroneous, due to a miscalculation. The value listed in Table 4.8 is the correct value.

Firstly, there are two values and corresponding differences that are noticeable. These values are the values for the vortex shedding Strouhal number, and the corresponding vortex shedding frequency, St and f_{vs}, respectively. These numbers are the sources of a 14.74 % and 15.12 % difference. This is most likely due to different methods of calculating the Strouhal number. The vibration response program presented in this thesis uses Eq. 2.34, which is for a triangular tube layout with a 30° layout angle, while Næss notes that his calculations are based on a 33.19 layout angle. Because of this, the Strouhal number will

naturally be different, and therefore also the vortex shedding frequency. This can be readily seen by considering Eq. 2.33.

The other compared values vary in difference from -4.34% to +2.08%. Some of these may be the result of differences in rounding, which is difficult to ascertain for certain. In addition to this, different pressure calculations may cause the difference in acoustic resonance frequency. For the purpose of this program, the pressure was defined as 1 atm, or 101.325 Pa. This was done for simplicity, and is an uncomplicated parameter to change. The critical velocity with regard to fluid-elastic instability, V_{cr}, is proportional to the tube's natural frequency. It is therefore natural for the deviation in natural frequency calculation to propagate into the critical velocity calculation as well. This deviation is most likely a result of the two different methods of calculating the natural frequency. While the natural frequency calculation in the vibration response program is based on the approach of Singh & Solér [19], which calculates the natural frequency of an N-span tube, the calculations by Næss were done in accordance with to ESDU's method of calculating the natural frequency of a singe span [17].

4.2.4 Comparison between different models

In this thesis, several different models and methods of calculation have been presented. In this section several of these will be implemented into the vibration response prediction program. The results will be compared to the original results, and the differences quantified.

Free vibration

Since the free vibration analysis is based on Singh & Solér's MULTSPAN program, a good way to verify the program output would be to compare it to their results. To do this, the program was run with the input parameters detailed in [19]. The resulting first three natural frequencies of the structure were in both cases 141.08 Hz, 206.01 Hz, and 249.54 Hz. The fact that all three natural frequencies are similar for both cases indicate that the calculations were implemented correctly. The resulting three mode shapes for both cases are compared in Fig. 4.5a and 4.5b.

As the figure shows, the mode shapes are highly similar in shape. The natural frequencies corresponding to each mode shape are indicated by numbers in the figure. With this, together with the similarity in frequencies, it is possible to conclude that the free vibration part of the vibration response prediction program is viable.

Fluid-elastic instability

As described previously, the vibration response prediction uses the so-called Connor's formula for calculating the critical velocity in relation to fluid-elastic instability. This formula is repeated below.

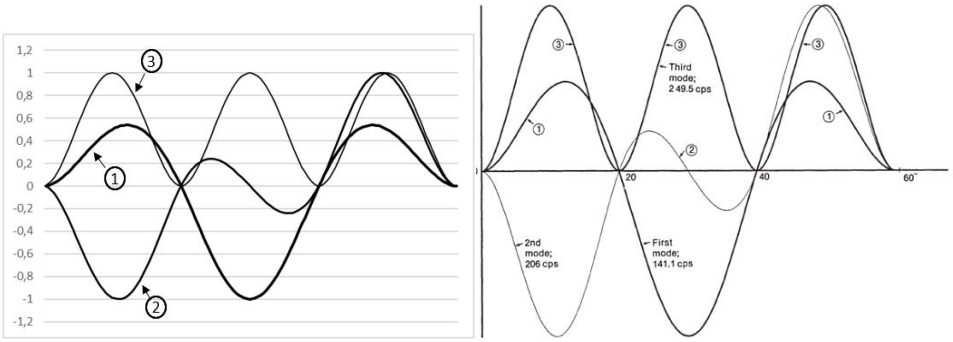

(a) Normalized mode shapes for a three-span tube. **(b)** Normalized mode shapes for a three-span tube. Reproduced from [19].

$$\frac{V_{cr}}{f_n D} = K(\frac{m\delta}{\rho D^2})^{\frac{1}{2}} \tag{4.7}$$

There has been some discussion regarding the fluid-elastic instability constant K. Among others, Pettigrew & Taylor suggest a value of 3.0 as a design criterion [20], while the HTFS Design Report No.25 [27] suggests a value of 3.3. As the HTFS Design Report has been used as a source of the program logic for the vibration response prediction program, the suggested value of 3.3 has been used. A K-value of 3.3 would also produce the highest critical velocity, which is important to consider when designing against it. The critical velocity is proportional to this constant, so the critical velocity when using Pettigrew & Taylors suggested value would naturally be 11 % lower than the one suggested by the HTFS Design Report.

Weaver & Fitzgerald [33] suggest that Connor's formula should be modified to account for differences in tube geometry. By separating experimental data into four different geometries, they established a different equation for each. For a normal triangular array, which is the type of array considered in the program, the equation is given by Eq. 4.8

$$\frac{V_{cr}}{f_n D} = 3.2(\frac{m\delta}{\rho D^2})^{0.4} \tag{4.8}$$

As the equation shows, the fluid-elastic instability constant K has a value of 3.2, and the right-side exponent is 0.4, as opposed to Connor's formula, where the exponent is 0.5.

By running the program with Weaver & Fitzpatrick's iteration of Connor's formula for normal triangular arrays, the resulting critical velocity for the first mode of vibration becomes 22.31 m/s. This is higher than the 18.11 m/s resulting from the original calculation. This means in effect that while both results suggest that there is no danger of fluid-elastic instability, Weaver & Fitzpatrick's formula reports an even lower probability.

Paidoussis [34] suggests another iteration of Connor's formula, which is given in Eq. 4.9 below. This version takes the pitch ratio, P_t/D, into account, something the other iterations do not include.

$$\frac{V_{cr}}{f_n D} = 5.8(\frac{m\delta}{\rho D^2})^{0.4}(\frac{P_t}{D} - 1)^{0.5} \tag{4.9}$$

After testing Paidoussis' version in the same manner as testing that of Weaver & Fitzpatrick, the critical velocity became 20.85 m/s for the first mode of vibration. This puts it in between the critical velocities from Eq. 2.42 and 4.8, and further emphasizes the importance of choosing a proper fluid-elastic instability model, even if all three velocities in this case are within the stable region.

Lift coefficient

As mentioned earlier, the fluctuating lift coefficient is estimated as a function of the pitch ratio P_t/D. The correlation is based upon a certain set of lift coefficients, and the correlation is found through linear interpolation. It is then important to check whether this estimation is supported by other previous works. A comparison of fluctuating lift coefficients of single cylinders in cross flow can be found in [6], as shown in Fig. 4.6 below.

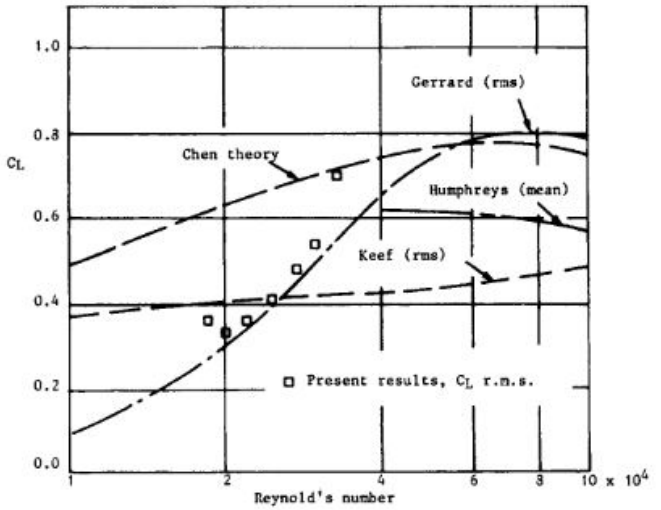

Figure 4.6: Fluctuating lift coefficient CL as a function of Reynolds number for a single tube in cross flow. Reproduced from [6].

The Reynolds number based on the input for the vibration response prediction program is estimated to be in the region of $6{\cdot}10^3$, which is low compared to figure. This is besides the point, however, because based on the previously established lift correlation, the lift coefficient should be constant for a certain pitch ratio – independent of the Reynolds number.

This is not the case for the measured values depicted in this figure, however, which shows a variation of C_L dependent on the Reynolds number. This may indicate that the correlation used in this program may not be as accurate as desired, and should be investigated further.

Despite this, there may be some cause to think that the lift coefficient obtained through the vibration response prediction program is within a realistic range. In Fig. 4.7, obtained from [7] is another graph of lift coefficients as a function of Reynolds numbers, collected from several different sources. This range of Reynolds numbers is between 1000 and 100 000, which means that the Reynolds number as used in the vibration response prediction program is within this range. The intersection between the Reynolds number and the lift coefficient from the output is indicated as the red lines in Fig. 4.7. This intersection is located above and to the left of a cluster of data points.

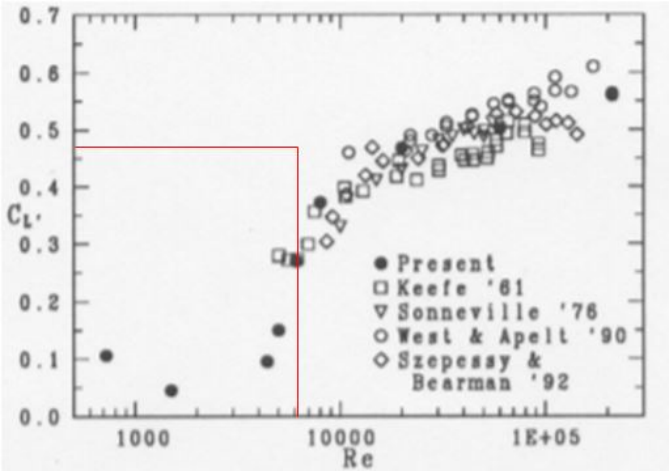

Figure 4.7: Fluctuating lift coefficient CL as a function of Reynolds number for a single tube in cross flow. Reproduced from [7].

As both Fig. 4.6 and 4.7 show, there may be a cause for concern regarding a lift coefficient based solely on the pitch ratio. While the output lift coefficient may be within a reasonable range of the ones indicated in Fig. 4.7, it is evident that the coefficient varies depending on the Reynolds number. The figure also shows that the lift coefficient obtained from the vibration response prediction will be within the data point cluster for a Reynolds number in the range $1{\cdot}10^4$ - $1{\cdot}10^5$. What this shows is that while the lift coefficient may not be in line with previous work, it fits with a reasonable degree for a wide range of Reynolds numbers.

Effective diameter

As previously mentioned, two methods of expressing the effective diameter of finned tubes have been proposed. One volumetrically based, D_{vol} and one hydraulic diameter based on the projected area of the finned tube, D_h. The equations for these diameters are given in

Eq. 2.27 and 2.28, respectively. The results of these calculations are D_{vol} = 15.77 mm and D_h = 14.60 mm. The program was rerun with D_{vol} as input instead of D_h, to check how this difference manifests in the vibration calculations. The results were a 48% change in maximum vortex shedding amplitude, a 12% change in the periodic shedding force, F_L, and an 18% change in the lift coefficient, C_L. The rest of the output remained unchanged. While the conclusions regarding vortex shedding, i.e., that the vortex shedding frequency was not sufficiently close to the natural frequency to make vortex shedding a problem, this shows that the choice of effective diameter must be made consciously to ensure accurate results.

5 Conclusion

A set of experiments was performed on an elliptical tube bundle with solid, rectangular fins. These were performed to measure heat transfer and pressure drop performance. The experiments were performed with varying Reynolds numbers, and corresponding Euler- and Nusselt correlations were calculated through regression analysis. The resulting correlations were, for the Euler numbers, within the range of comparable previous work [1]. For the Nusselt numbers the results were outside this range, where the exponent of the Reynolds number in the correlation were significantly lower than that of previous work [32]. This may have been the result of fouling on the water side of the tubes.

A two-part vibration response prediction program was also created in Fortran 90. The first part was created to evaluate the free vibration response of an N-span tube, where the aim was to find the first N natural frequencies and corresponding mode shapes of the tube. The second part was created to evaluate the risk of four forced vibration mechanisms: vortex induced vibration, fluid-elastic instability, turbulent buffetting and acoustic resonance. The output of the program was then compared to that of previous work, where both the free vibration and forced vibration parts were found to be in good agreement with these [17], [19]. There was, however, some variation in the results when different models were tested. This program may aid further vibration analysis of compact heat exchanger units.

6 Further Work

As there is limited data regarding heat transfer in compact heat exchanger units with similar geometry as the one considered in this thesis, it would be beneficial to do more such experiments. A deeper theoretical understanding would enable the optimization of such heat exchangers for a larger variety of cases. This would enable the creation of geometries specific for elliptical tubes, so that optimal geometries can be identified.

As the results of the heat transfer experiments suggest, there may be fouling on the tube side area. If this is the case, this fouling may have caused extra thermal resistance to occur, which in turn will have influenced the results. Because of this, measures should be taken to remove the fouling, and additional experiments should be performed to verify the results.

The forced vibration part of the vibration response program is designed to simulate a constant velocity distribution. Because of this, it is not a realistic representation of a compact heat exchanger. The reason for this is that the fluid velocity, and therefore the fluid forces will vary inside a shell and tube heat exchanger. The velocity will typically be higher at both the shell-side inlet and outlet. In effect, this would mean that some spans will have more fluid forces acting on it than others. The program should, because of this, be expanded by implementing a varying velocity distribution. This would serve to identify the points of the tube that are more susceptible to critical vibration.

Shell-and-tube heat exchangers are often composed of not only straight tubes but also u-bend regions. This means that the tubes at some point turn 180 degrees, which the program does not account for. These u-bend regions complicate the vibration analysis, as this enables out-of-plane vibration of the tubes, in addition to the already existing in-plane vibration. A natural further step in the program would then be to account for the out-of-plane vibration. This function was originally meant to be included in the vibration response prediction program, but due to the complexity of the calculations and strict time limitations, this was not implemented.

Bibliography

[1] A Holfeld. Experimental investigation of heat transfer and pressure drop in compact waste heat recovery units. Master's thesis, Norwegian University of Science and Technology, 2016.

[2] Dewitt D.P. Bergman T.L. Incropera, F.P. and A.S. Lavine. *Principles of HEAT and MASS TRANSFER*. John Wiley & Sons, 7th edition, 2013.

[3] Thiago A Fiorentin, Alexandre Mikowski, Olavo M Silva, and Arcanjo Lenzi. Noise and vibration analysis of a heat exchanger: a case study. *International Journal of Acoustics and Vibration*, 22(2):270–275, 2017.

[4] Flow around objects (n.d.). `http://www.et4u.org/Toy_information/Cylinder_flow.html`. Accessed: 2018-11-18.

[5] D.S. Weaver and L.K. Grover. Cross-flow induced vibrations in a tube bank—turbulent buffeting and fluid elastic instability. *Journal of Sound and Vibration*, 59(2):277 – 294, 1978.

[6] K.C. Shim, R.S. Hill, and R.I. Lewis. Fluctuating lift forces and pressure distributions due to vortex shedding in tube banks. *International Journal of Heat and Fluid Flow*, 9(2):131 – 146, 1988.

[7] Christoffer Norberg. Pressure forces on a circular cylinder in cross flow. 09 1992.

[8] Global warming of 1.5 c : an ipcc special report on the impacts of global warming of 1.5 c above pre-industrial levels and related global greenhouse gas emission pathways, in the context of strengthening the global response to the threat of climate change, sustainable development, and efforts to eradicate poverty, 2018.

[9] Hao Peng and Xiang Ling. Analysis of heat transfer and flow characteristics over serrated fins with different flow directions. *Energy Conversion and Management*, 52(2):826 – 835, 2011.

[10] Vikram B Yadav, SR Desai, and MM Mirza. Review on fluid-elastic instability in finned tube arrays, 2013.

[11] W.A. Mair, P.D.F. Jones, and R.K.W. Palmer. Vortex shedding from finned tubes. *Journal of Sound and Vibration*, 39(3):293 – 296, 1975.

[12] Robert H. Lumsden and David S. Weaver. The effect of fins on fluidelastic instability in in-line and rotated square tube arrays. *Journal of Pressure Vessel Technology*, 132(5), 2010.

[13] Michael Fischer. Flow-induced vibration in spiral finned gas tube bundle heat exchangers. pages 253–259, 2003.

[14] Erling Næss. An experimental study of heat transfer and pressure drop in serrated-fin tube bundles and investigation of particulate fouling in waste heat recovery heat exchangers, 2007.

[15] Shigehiko Kaneko, Tomomichi Nakamura, Fumio Inada, Minoru Kato, Kunihiko Ishihara, Takashi Nishihara, and Mikael A. Langthjem, editors. *Chapter 2 - Vibration Induced by Cross-Flow*. Academic Press, Oxford, 2014.

[16] M. Eid and S. Ziada. Vortex shedding and acoustic resonance of single and tandem finned cylinders. *Journal of Fluids and Structures*, 27(7):1035 – 1048, 2011.

[17] Erling Næss. Flow-induced vibrations in waste heat recovery units - a review, 2017.

[18] M.J. Pettigrew, Y. Sylvestre, and A.O. Campagna. Vibration analysis of heat exchanger and steam generator designs. *Nuclear Engineering and Design*, 48(1):97 – 115, 1978. Special Issue Structural Mechanics in Reactor Technology - Smirt-4.

[19] K.P. Singh and A.I. Soler. *Mechanical design of heat exchangers and pressure vessel components*. Arcturus Publishers, 1984.

[20] M.J. Pettigrew and C.E. Taylor. Vibration analysis of shell-and-tube heat exchangers: an overview—part 2: vibration response, fretting-wear, guidelines. *Journal of Fluids and Structures*, 18(5):485 – 500, 2003. Arrays of Cylinders in Cross-Flow.

[21] Jeffrey McClure and Serhiy Yarusevych. Vortex shedding and structural loading characteristics of finned cylinders. *Journal of Fluids and Structures*, 65:138 – 154, 2016.

[22] S.J. Price. A review of theoretical models for fluidelastic instability of cylinder arrays in cross-flow. *Journal of Fluids and Structures*, 9(5):463 – 518, 1995.

[23] B.J. Ledger. Fluidelastic instability of tube arrays subjected to axisymmetric jet flow. Master's thesis, McMaster University, 2015.

[24] R.D. Blevins and M.M. Bressler. Acoustic resonance in heat exchanger tube bundles—part ii: Prediction and suppression of resonance. *Journal of Pressure Vessel Technology*, 109:282–288, 1987.

[25] L.K. Grover and D.S. Weaver. Cross-flow induced vibrations in a tube bank—vortex shedding. *Journal of Sound and Vibration*, 59(2):263 – 276, 1978.

[26] P. R. Owen. Buffeting excitation of boiler tube vibration. *Journal of Mechanical Engineering Science*, 7(4):431–439, 1965.

[27] A.O. Campagna, J.J. McMonagle, and M.J. Pettigrew. Heat transfer and fluid flow service design report no.25. pipo1: Heat exchanger tube vibration, 1988.

[28] Jaemin Kim, Byoung Ik Choi, Kuisoon Kim, Man Yeong Ha, Changmin Son, and Sang Youl Yoon. Acoustic resonance and pressure drop through a staggered tube bundle in a compact heat exchanger. *International Journal of Heat and Mass Transfer*, 91:63 – 67, 2015.

[29] S. Ziada, A. Oengören, and E.T. Bühlmann. On acoustical resonance in tube arrays part ii: Damping criteria. *Journal of Fluids and Structures*, 3(3):315 – 324, 1989.

[30] Measurement of fluid flow by means of pressure differential devices, inserted in circular cross-section conduits running full. part 1: General principles and requirements (iso 5167-1:2003)".

[31] Measurement of fluid flow by means of pressure differential devices, inserted in circular cross-section conduits running full. part 2: Orifice plates (iso.

[32] S Huang and S Pu. Convection and heat transfer of elliptical tubes. *Heat and Mass Transfer*, 30(6):411–415, 1994.

[33] D.S. Weaver and J.A. Fitzpatrick. A review of cross-flow induced vibrations in heat exchanger tube arrays††the original version of this paper was prepared for presentation at the international conference on flow induced vibrations, bowness-on-windermere, 12–14 may 1987; proceedings published by bhra the fluid engineering centre, cranfield, england (ed. r. king). *Journal of Fluids and Structures*, 2(1):73 – 93, 1988.

[34] M.P. Païdoussis, S.T. Price, T. Nakamura, B. Mark, and W. Njuki Mureithi. Flow-induced vibrations and instabilities in a rotated-square cylinder array in cross-flow. *Journal of Fluids and Structures*, 3(3):229 – 254, 1989.

Appendix

A Vibration response prediction program

In the appendix can be found the output screen of the vibration response prediction program, along with the Fortran 90 code in its entirety.

```
-------------------- Natural frequencies --------------------

F, 1 , =   18.1759664472221445  Hz
F, 2 , =   20.5183505681702663  Hz
F, 3 , =   27.4707977195335182  Hz
F, 4 , =   36.3350216432490143  Hz

-------------------- Fluid-elastic instability --------------------

Critical velocity 1 =  18.1065281048830826 m/s | Ur/Ucrit =    0.9388878917883398
No danger
Critical velocity 2 =  20.4399635258568573 m/s | Ur/Ucrit =    0.8317040281649597
No danger
Critical velocity 3 =  27.3658499764841991 m/s | Ur/Ucrit =    0.6212122047956962
No danger
Critical velocity 4 =  36.1962095652730014 m/s | Ur/Ucrit =    0.4696624371494955
No danger

-------------------- VORTEX SHEDDING --------------------

FL =    0.4688361469503877  N/m | CL =    0.4629767136622780
Ymax =    3.2872922389476636E-03  m
Fvs/Fn 1 =  15.1608649715345560
Vortex shedding is not a problem
Fvs/Fn 2 =  13.4300938137275967
Vortex shedding is not a problem
Fvs/Fn 3 =  10.0311383690737959
Vortex shedding is not a problem
Fvs/Fn 4 =   7.5839606135112021
Vortex shedding is not a problem
Strouhal number, Sr =    0.2366603086052219
Vortex shedding frequency, fvs =    2.7556337303347760E+02  Hz

-------------------- Acoustic resonance --------------------

fa/fvs =    0.1791153233146724
No danger of acoustic resonance
Nx =    1.6426159143447876 fa =   49.3576226545730350

-------------------- Turbulent Buffetting --------------------

Maximum RMS amplitude, Turbulent Buffetting =    5.3162974570430477E-05  m
```

Figure 6.1: Example of vibration response prediction program output screen.

```
MODULE felles
implicit none
  INTEGER :: N = 3
  double precision :: pi = 3.14159
  double precision :: tubelength = 4.1
  double precision :: Uniformflow = 1.0
  double precision :: Lm,VM,FR,FS
  double precision, dimension(:), allocatable :: X
  double precision, dimension(:), allocatable :: ELL
  double precision,dimension(:), allocatable :: UCRIT,XKAPPA,FRENAT
  double precision,dimension(:,:),allocatable :: B,C,D,XVECT
   SAVE X,UCRIT,XKAPPA,FRENAT,N,ELL,pi,Lm,B,C,D,VM,FR,FS,XVECT

END MODULE felles

program vibresponse
use felles
IMPLICIT DOUBLE PRECISION (A-H,O-Z)
double precision :: eiv,AMOM,F,AKAP,RHOT,RHOF,D1,D2,DF,FD,T,PF,PT,VINF,L
double precision :: AMOMeff = 6.75D-10  !Second moment of area
double precision :: YM = 193000.0D6     !Young's Modulus
double precision :: SPMID = 0.9         !Mid-span length
VM = 1.411                              !Virtual mass
SPEND = 0.9                             !End-span length
eiv = sqrt(YM*AMOMeff/VM)

allocate(XVECT(N,N))
allocate(ELL(N))
allocate(UCRIT(N))
allocate(XKAPPA(N))
allocate(FRENAT(N))
allocate(B(3*N,N))
allocate(C(3*N,N))
allocate(D(3*N,N))
allocate(X(3*N))
do 999 I = 1,(3*N)
      X(I) = 0
999 continue
ELL(N) = SPEND
ELL(1) = SPEND
      do 69 I = 2,(N-1)
```

```
ELL(I) = SPMID
69 continue


call natfre(N,eiv,F,AKAP)
call instability(Vcrit,17.00D0,0.031D0,0.48D0)
call vortexshedding(0.48D0,14.6D-3,17.0D0,0.03566D0)
Yturb = turbulentbuffetting(SPMID)
print*,"         "
print*, "-------------------- Turbulent Buffetting --------------------"
print*,"         "
print*, "Maximum RMS amplitude, Turbulent Buffetting = ",Yturb, " m"

end program vibresponse

subroutine natfre(N,eiv,F,AKAP)
      USE felles, ONLY : ELL,X,pi,UCRIT,Lm,FRENAT,XKAPPA,B,C,D
      implicit double precision (A-H,O-Z)
      double precision :: HIGHELL = 0.0
      integer :: ISOL = 0
      print*,"         "
      print*, "-------------------- Natural frequencies
--------------------"
      print*,"         "
      do 111 I = 1,N
111 HIGHELL = DMAX1(HIGHEll,ELL(I))
      X1 = 3.0/HIGHELL
      X2 = 1.01*X1
      Y1 = calc(X1,0,ELL,N)
      do 150 I = 1, 1000
      Y2 = calc(X2,0,ELL,N)
      IF (Y1*Y2) 105,105,110
105 X3 = 0.5*(X2+X1)
      IF(ABS(X3-X2) <= 5.0E-06) go to 130
      Y3 =calc(X3,0,ELL,N)
      IF(Y2*Y3) 115,115,120
115 X1 = X2
120 X2 = X3
      Y2 = Y3
      go to 105
130 ISOL = ISOL+1
      AKAP = X3
```

```
      F = AKAP*AKAP*eiv/(2.0*pi)
      DUMP = CALC(X3,1,ELL,N)
!Kompilerer ikke riktig uten.
      XKAPPA(ISOL)=AKAP
      FRENAT(ISOL)=F

     DO 2001 J=1,N
        J3=3*J
        B(ISOL,J)=X(J3-1)
        C(ISOL,J)=X(J3-2)
        D(ISOL,J)=X(J3)
 2001  CONTINUE



      print*, 'F,',ISOL,', = ', F, ' Hz'
      Y = calc(X3,1,ELL,N)
      call modeshape(AKAP)
      if (ISOL == N) go to 160
      X2 = DMAX1(X1,X2)
110 X1=X2
      X2 = 1.01*X2
      Y1=calc(X1,0,ELL,N)
150 continue
160 continue!stop

end subroutine natfre


subroutine modeshape(AKAP)
use felles, only : ELL,X,N
implicit double precision (A-H,O-Z)


dimension YY(50),ZZ(50)

CS(Z) = COS(AKAP*Z) - COSH(AKAP*Z)
S(Z)  = SIN(AKAP*Z) + SINH(AKAP*Z)
SS(Z) = SIN(AKAP*Z) - SINH(AKAP*Z)
T=0.0
Y=0.0
open(unit = 10,file='C:\Users\thoma\OneDrive\Desktop\vib.txt')
```

```
701 FORMAT(X,10E12.4)
do 101 I = 1,N
I3 = 3*I
do 201 J = 1,50
W = ELL(I)*0.02*J
Y = X(I3-1)*CS(W)+X(I3-2)*S(W) + X(I3)*SS(W)
T = T+0.02*ELL(I)
ZZ(J) = T
YY(J) = Y
write(10,*)Y


201 continue
!write(6,702)
!702 FORMAT(//,10(2H**),"MODE SHAPE",5(2H**),/,5(12X,"X",10X,"Y",3X))
!write(6,700) (ZZ(J),YY(J),J=1,50)
!700 FORMAT(5(6X,F9.3,2X,E10.3))
101 continue
return

end subroutine modeshape



function calc(AKAP,ISOLV,ELL,N)
use felles, only : X
implicit double precision (A-H,O-Z)
dimension A(3*N-1,3*N-1), ELL(N), G((3*N-1)*(3*N-1))

C(I)  = cos(AKAP*ELL(I)) + cosh(AKAP*ELL(I))
CS(I) = cos(AKAP*ELL(I)) - cosh(AKAP*ELL(I))
S(I)  = sin(AKAP*ELL(I)) + sinh(AKAP*ELL(I))
SS(I) = sin(AKAP*ELL(I)) - sinh(AKAP*ELL(I))

DO 1 I=1,(3*N-1)
       DO 2 J=1,(3*N-1)
        G((3*N-1)*(I-1)+J) = 1.0
        A(I,J) = 0.0
 2     CONTINUE
 1    CONTINUE
```

```
if(N == 1) go to 220

do 120 I = 1,(N-1)
      J = 1+(I-1)*3
      A(J,J)            = CS(I)
      A(J,J+1)    = SS(I)
      A(J+1,J+1)  = -S(I)
      A(J+1,J)    = -C(I)
      A(J+1,J+3)  = 2.0
      A(J+2,J+2)  = -2.0
      A(J+2,J)    = -S(I)
      A(J+2,J+1)  = CS(I)

120 CONTINUE

if (N < 3) go to 210

do 1300 I = 2,(N-1)
      J = 1+(I-1)*3
      A(J,J-1)    = S(I)
      A(J+1,J-1)  = -SS(I)
      A(J+2,J-1)  = C(I)

1300 CONTINUE
210 CONTINUE
      A(3*N-1,3*N-3) = C(N)
      A(3*N-2,3*N-3) = S(N)
220   A(3*N-1,3*N-1) = CS(N)
      A(3*N-1,3*N-2) = -S(N)
      A(3*N-2,3*N-2) = CS(N)
      A(3*N-2,3*N-1) = SS(N)

      N3M = 3*N-1-ISOLV

do 31 J = 1,N3M
 do 30 I = 1,N3M
      NDEX = (N3M*(J-1)+I)
      G(NDEX) = A(I,J)
30 continue
31 continue
```

```
call minv(G,N3M,N3M**2,CALC)

if(ISOLV == 0) RETURN

do 41 J = 1,N3M
do 40 I = 1,N3M
      NDEX = (N3M*(J-1)+I)
      A(I,J) = G(NDEX)
40 continue
41 continue

      F = -SS(N)

do 300 I = 2,(N3M+1)

      X(I) = A(I-1,N3M)*F

300 CONTINUE

      X(1)  = 0.0
      X(3*N)      = 1.0

RETURN
end function


SUBROUTINE MINV(A,N,N2,D)                        !?

      IMPLICIT DOUBLE PRECISION (A-H,O-Z)


      DIMENSION L(N),M(N), A(N2)

      D = 1.0
      NK = -N
      DO 80 K=1,N
      NK = NK+N
      L(K) = K
      M(K) = K
      KK = NK+K
      BIGA = A(KK)
      DO 21 J=K,N
```

```
      IZ = N*(J-1)
      DO 20 I = K,N
      IJ = IZ+I
10    IF(ABS(BIGA)-ABS(A(IJ))) 15,20,20
15    BIGA = A(IJ)
      L(K) = I
        M(K) = J
20    CONTINUE
21    CONTINUE !mrk
      J = L(K)
      IF(J-K) 35,35,25
25    KI = K-N
      DO 30 I=1,N
      KI = KI+N
      HOLD = -A(KI)
      JI = KI-K+J
      A(KI) = A(JI)
30    A(JI) = HOLD
35    I = M(K)
      IF(I-K) 45,45,38
38    JP = N*(I-1)
      DO 40 J=1,N
      JK= NK+J
      JI = JP+J
      HOLD = -A(JK)
      A(JK) = A(JI)
40    A(JI) = HOLD
45    IF(BIGA) 48,46,48
46    D = 0.0
      RETURN
48    DO 55 I=1,N
      IF(I-K) 50,55,50
50    IK = NK+I
      A(IK) = A(IK)/(-BIGA)
55    CONTINUE
      DO 65 I=1,N
      IK = NK+I
      HOLD = A(IK)
      IJ = I-N
      DO 65 J=1,N
      IJ = IJ+N
      IF(I-K) 60,65,60
```

```
60    IF(J-K) 62,65,62
62    KJ = IJ-I+K
      A(IJ) = HOLD*A(KJ)+A(IJ)
65    CONTINUE
      KJ = K-N
      DO 75 J=1,N
      KJ = KJ+N
      IF(J-K) 70,75,70
70    A(KJ) = A(KJ)/BIGA
75    CONTINUE
      D = D*BIGA
      A(KK) = 1.0/BIGA
80    CONTINUE
      K=N
100   K = K-1
      IF(K) 150,150,105
105   I = L(K)
      IF(I-K) 120,120,108
108   JQ = N*(K-1)
      JR = N*(I-1)
      DO 110 J=1,N
      JK = JQ+J
      HOLD = A(JK)
      JI = JR+J
      A(JK) = -A(JI)
110   A(JI) = HOLD
120   J = M(K)
      IF(J-K) 100,100,125
125   KI = K-N
      DO 130 I=1,N
      KI = KI+N
      HOLD = A(KI)
      JI = KI-K+J
      A(KI) = -A(JI)
130   A(JI) = HOLD
      GOTO 100
150   CONTINUE

      RETURN
      END
```

```
!_____________________________________________________________________
_____________________________________________________

subroutine vortexshedding(rhoair,dh,Vr,Pt)
use FELLES,only : ELL,pi,X,N,UCRIT,Lm,FRENAT,XKAPPA,tubelength,VM,B,C,D
implicit double precision (A-H,O-Z)

)
CC(Z)  = COS(AKAP*Z) + COSH(AKAP*Z)
CS(Z) = COS(AKAP*Z) - COSH(AKAP*Z)
S(Z)  = SIN(AKAP*Z) + SINH(AKAP*Z)
SS(Z) = SIN(AKAP*Z) - SINH(AKAP*Z)
vdist = 1.0
DampC = 0.031*2.0*VM
delta = 0.031
Constant=VM/(2.0*pi*DampC)

if (Pt/dh < 1.6) then
      CL = 0.075
else if(Pt/dh > 2.5) then
      CL = 0.49
else
      CL = (0.461*Pt/dh)-0.663
end if

FL = CL*rhoair*dh*Vr*Vr/2.0
Ymax=0.0
Xmodmax = 0.0
xpos=0.0


if (N==1.0) then
Ymax = FL/(pi*pi*FRENAT(1)*FRENAT(1)*VM*delta)


else
do 301 K = 1,N                                          !Iteration over mode
      AKAP = XKAPPA(K)
      do 101 I = 1,N                                    !Iteration over spans
      I3 = 3*I
            do 201 J = 1,50   !Iteration in 1/50 increments over each span
            W = ELL(I)*0.02*J
```

```
            Y = B(K,I)*CS(W)+C(K,I)*S(W) + D(K,I)*SS(W)     !Mode shape

            xmod =
(X(I3)*SS(ELL(I))+X(I3)*CS(ELL(I))-X(I3)*(CC(ELL(I))-2.0))/AKAP!Integral of
modeshape

            V = (FL*Y)/(FRENAT(K)*FRENAT(K)*4.0*pi*delta*VM)

      if (abs(V)>abs(Ymax)) then
            Ymax = V
            xpos = W
            Span = I
            mode = K
      end if
      if(abs(Y) > abs(xmodmax)) then
      xmodmax = abs(Y)
      end if



201 continue
101 continue
301 continue
end if
print*,"         "
print*,"-------------------- VORTEX SHEDDING --------------------"
print*,"         "
print*,"FL = ",FL," N/m | ","CL = ",CL
print*, 'Ymax = ', abs(Ymax), " m"

SrVS = (1.0/1.73)*(dh/Pt)

fvs = Vr*SrVS/dh

do 6666 I =1,N
print*, "Fvs/Fn",I,"=",fvs/FRENAT(I)
if ( fvs < 1.2*FRENAT(I) .AND. fvs < 0.8*FRENAT(I)) then
      print*, "Danger of vortex shedding"
            else
                  print*,"No danger"
end if
6666 continue
```

```
print*, "Strouhal number, Sr = ",SrVS
print*, "Vortex shedding frequency, fvs = ",fvs, " Hz"
print*,"          "
print*, "--------------------- Acoustic resonance --------------------"
print*,"          "

call acousticresonance(fvs,fa,sigma,vdist,supmode)
print*,"fa = ",fa
end


subroutine instability(Vcrit,Vr,delta,rhoG)
use FELLES
implicit double precision (A-H,O-Z)
print*,"          "
print*,"--------------------- Fluid-elastic instability
--------------------"
print*,"          "
do I = 1,N
if (uniformflow == 2.0) then

      Vcrit = FRENAT(I)*3.3*((delta*VM)/(rhoG))**0.5

else

      Vcrit =
3.3*((delta*FRENAT(I)*FRENAT(I))/rhoG*squareintegral(XKAPPA(I),ELL(I))**0.5
)
      print*, squareintegral(XKAPPA(I),tubelength)
end if

if (Vr > Vcrit) then

      print*, "Critical velocity", I, "=",Vcrit,"m/s"," | ", "Ur/Ucrit =
",Vr/Vcrit
      print*, "Danger of instability"
else
      print*, "Critical velocity", I, "=",Vcrit,"m/s"," | ", "Ur/Ucrit =
",Vr/Vcrit
```

```
      print*, "No danger"

end if
end do

end subroutine
```

```
double precision function turbulentbuffetting(xpos)
!The main program for calculating turbulent buffetting amplitude.
!Returns the maximum RMS amplitude.
!Sums the effect of each excited mode over all spans.
!I,J  signifies modes R and S
!M signifies span number
!K signifies span increments in 50 increments per span, to sum over all
modes per increment.
use FELLES
implicit double precision (A-H,O-Z)
EXTERNAL TBFORC

       DO 6300 I=1,N
        DO 6200 J=I,N
          FLOW=0.0
          FINT=0.0
          DO 6100 K=1,N
            FHIGH=FRENAT(K)
            IF(MOD(K,2) .EQ. 0) FHIGH=0.5*(FRENAT(K)+FRENAT(K-1))
            FR=FRENAT(I)
            FS=FRENAT(J)
            CALL QGAUS(TBFORC,flow,fhigh,t4)
            FINT=FINT+T4
            IF(I .NE. J) FINT=FINT+T4
            FLOW=FHIGH
 6100     CONTINUE
          XVECT(I,J) = FINT

 6200   CONTINUE
```

```
 6300 CONTINUE


 ampltb =0.0
 POSX = 0.0
 do 40 M=1,N
    dx=ELL(M)/50
    POSX=0.0
      do 30 K = 1,50
      SUM=0.0
    POSX=POSX+DX
      do 10 I = 1,N
            xmoder = (B(I,M)*(cos(XKAPPA(I)*POSX)-cosh(XKAPPA(I)*POSX)) &
                        +
C(I,M)*(sin(XKAPPA(I)*POSX)+sinh(XKAPPA(I)*POSX))+D(I,M)*(sin(XKAPPA(I)*POS
X)-sinh(XKAPPA(I)*POSX)))/FRENAT(I)
            do 20 J = 1,N
              xmodes = (B(J,M)*(cos(XKAPPA(I)*POSX)-cosh(XKAPPA(I)*POSX))&
               + C(J,M)*(sin(XKAPPA(I)*POSX)+sinh(XKAPPA(I)*POSX)) +
D(J,M)*(sin(XKAPPA(I)*POSX)-sinh(XKAPPA(I)*POSX)))/FRENAT(J)
              SUM = SUM +
XVECT(I,J)*abs(xmoder*xmodes)*wf(B(I,M),C(I,M),D(I,M),B(J,M),C(J,M),D(J,M),
Lm,XKAPPA(I))/(16.0*(pi)**4.0)

                        20 continue
                  10 continue
      if(SUM>ampltb)then
      ampltb = SUM
      end if
30 continue
40 continue

turbulentbuffetting = ampltb

end function turbulentbuffetting

double precision function wf(B1,C1,D1,B2,C2,D2,xmax,AKAP)
!Serves the purpose of returning the integral Ør(x)*Øs(x')dxdx' from 0 to
xmax.
!Is the part of the weighting function that is dependent on axial position.
!Is a part of the calculation of turbulent buffetting amplitude.
use FELLES
```

```
implicit double precision (A-H,O-Z)


            !Integral of modeshape from 0 to Lm
int1 =
(C1*(sin(AKAP*xmax)+sinh(AKAP*xmax))+D1*(sin(AKAP*xmax)-sinh(AKAP*xmax))-B1
*(cos(AKAP*xmax)-cosh(AKAP*xmax)-2.0))


int2 =
(C2*(sin(AKAP*xmax)+sinh(AKAP*xmax))+D2*(sin(AKAP*xmax)-sinh(AKAP*xmax))-B2
*(cos(AKAP*xmax)-cosh(AKAP*xmax)-2.0))

wf = int1*int2

end function

SUBROUTINE QGAUS(FUNC,A,B,SS)

!Integrates a specified function FUNC between boundaries A and B. Returns
SS
!Used to integrate Hr(f)Hs(f)S(f) from 0 to infinity.


IMPLICIT DOUBLE PRECISION(A-H,O-Z)


double precision, dimension(5) :: X,WX =
(/0.1488743389,0.4333953941,0.6794095682,0.8650633666,0.9739066285/)
W = (/0.295524227,0.2692667193,0.2190863625,0.1494513491,0.0666713443/)

      XM=0.5*(B+A)
      XR=0.5*(B-A)
      SS=0.0
      DO 1000 J=1,5
        DX = XR*X(J)
        SS=SS+W(J)*(FUNC(XM+DX)+FUNC(XM-DX))
 1000 CONTINUE
      SS = XR*SS

return
end
```

```
double precision function squareintegral(AKAP,XPOS)
use FELLES,only : ELL,pi,N,UCRIT,Lm,X,FRENAT,XKAPPA,tubelength
!Calculates the integral of the square of the mode shape, from 0 to Lm.
     implicit double precision (A-H,O-Z)
      B = X(3*N-1)
      C = X(3*N-2)
      D = X(3*N)
      Y=(AKAP*XPOS)

      VAL1=(SIN(2.*Y)+2.*Y)/(4.*AKAP)

      VAL2=(2.0*Y-SIN(2.*Y))/(4.0*AKAP)

      VAL3=(1.0-COS(2.0*Y))/(4.0*AKAP)

      VAL4=(COS(Y)*SINH(Y)+SIN(Y)*COSH(Y))/(2.0*AKAP)

      VAL5=(COS(Y)*COSH(Y)+SIN(Y)*SINH(Y)-1.0)/(2.0*AKAP)

      VAL6=(SIN(Y)*SINH(Y)-COS(Y)*COSH(Y)+1.0)/(2.0*AKAP)

      VAL7=(SIN(Y)*COSH(Y)-COS(Y)*SINH(Y))/(2.0*AKAP)

      VAL8=(SINH(2.0*Y)+2.0*Y)/(4.0*AKAP)

      VAL9=(DCOSH(2.0*Y)-1.0)/(4.0*AKAP)

      VAL10=(DSINH(2.0*Y)-2.0*Y)/(4.0*AKAP)

      F1 = (B*B)*VAL1
      F2 = (C+D)*(C+D)*VAL2
      F3 = 2.0*(B*C + B*D)*VAL3
      F4 = -2.0*(B*B)*VAL4
      F5 = 2.0*(B*C - B*D)*VAL5
      F6 = -2.0*(B*C + B*D)*VAL6
      F7 = 2.0*(C*C - D*D)*VAL7
      F8 = (B*B)*VAL8
      F9 = 2.0*(B*D - B*C)*VAL9
      F10= (C-D)*(C-D)*VAL10
squareintegral=F1+F2+F3+F4+F5+F6+F7+F8+F9+F10

end function squareintegral
```

```
double precision function TBFORC(F)
use felles
implicit double precision (A-H,O-Z)

DampC = 0.031*2*pi

!           Frequency response function for mode r
    HR = 1.0-(F/FR)**2.0                                    !Real
    HRI = DampC*F/(2.0*pi*VM*FR)                            !Imaginary
      HRZ=(HR**2.0 + HRI**2.0)**(-0.5)                      !Absolute value
    THETAR=DATAN2(HRI,HR)                                   !Angle

!           Frequency response function for mode s

    HS = 1.0-(F/FS)**2.0                                    !Real
    HSI = DampC*F/(2.0*pi*VM*FS)                            !Imaginary
    HSZ=(HS**2.0 + HSI**2.0)**(-0.5)                        !Absolute value
    THETAS=DATAN2(HSI,HS)                                   !Angle
        IF(F .LE. 40.0) THEN
         CRFAC = 24.0D-03
        ELSE
         CRFAC = 32.6*F**(-1.96)
        ENDIF

 TBFORC = HRZ*HSZ*cos(THETAR-THETAS)*CRFAC**2.0 !Weightingfunction(F)

end function TBFORC



subroutine acousticresonance(fvs,fa,sigma,xmode,supmode)
use felles
implicit double precision (A-H,O-Z)

Vtot = 0.03566*0.03257                                          !=Pt*Pl

Vtube = pi*0.01238*0.01238*0.25
!=pi*d2*d2*0.25

Vfin = (pi*1.05D-3*0.00935*0.1238)/(2.0*8.98D-3)      !=(pi*tf*hf*D2)/(sf)
```

```
sigma = (Vfin+Vtube)/Vtot

c0 = sqrt(1.4*101325.00/0.48)
!=sqrt(1.4*Pair/rhoair) /pressure 1 atm

ceff = c0/(1.0+sigma)

print*, "fa/fvs = ",fa/fvs

if ( fa/fvs < 0.8 .OR. fa/fvs > 1.35) then

      print*, "No danger of acoustic resonance"

else

      print*, "Danger of acoustic resonance"

end if


end subroutine
```

NTNU SINTEF

Risk Assessment Report

Ribberør Rig

Prosjektnavn	Heat transfer and pressure drop in finned tube bundles
Apparatur	Ribberør Rig
Enhet	NTNU
Apparaturansvarlig	Erling Næss
Prosjektleder	Erling Næss
HMS-koordinator	Morten Grønli
HMS-ansvarlig (linjeleder)	Terese Løvås
Plassering	VATL- 'Fellesverksted' Mesanin
Romnummer	
Risikovurdering utført av	Anna Holfeld, Erik Langørgen, Morten Grønli

Approval:

	Navn	Dato	Signatur
Prosjektleder	Erling Næss		
HMS koordinator	Morten Grønli		
HMS ansvarlig (linjeleder)	Terese Løvås		

NTNU SINTEF

TABLE OF CONTENTS

1 INTRODUCTION

The aim of this project is to gain knowledge about heat transfer and pressure drop in finned tube heat exchangers. This knowledge shall be used for the design of compact waste heat recovery units.

The experimental rig is located at/on the mezzanine in the thermal laboratory.

2 CONCLUSION

The experimental setup is approved

Apparaturkort (UNIT CARD) is valid for **12 months**
Forsøk pågår kort (EXPERIMENT IN PROGRESS) is valid for **12 months**

3 ORGANISATION

Rolle	
Prosjektleder	Erling Næss
Apparaturansvarlig	Erling Næss
Romansvarlig	Paul Svendsen
HMS koordinator	Morten Grønli
HMS ansvarlig (linjeleder):	Terese Løvås

4 RISK MANAGEMENT IN THE PROJECT

Hovedaktiviteter risikostyring	Nødvendige tiltak, dokumentasjon	DATE
Prosjekt initiering	Prosjekt initiering mal	
Veiledningsmøte Guidance Meeting	Skjema for Veiledningsmøte med pre-risikovurdering	
Innledende risikovurdering Initial Assessment	Fareidentifikasjon – HAZID Skjema grovanalyse	
Vurdering av teknisk sikkerhet Evaluation of technical security	Prosess-HAZOP Tekniske dokumentasjoner	
Vurdering av operasjonell sikkerhet Evaluation of operational safety	Prosedyre-HAZOP Opplæringsplan for operatører	
Sluttvurdering, kvalitetssikring Final assessment, quality assurance	Uavhengig kontroll Utstedelse av apparaturkort Utstedelse av forsøk pågår kort	

5 DESCRIPTIONS OF EXPERIMENTAL SETUP

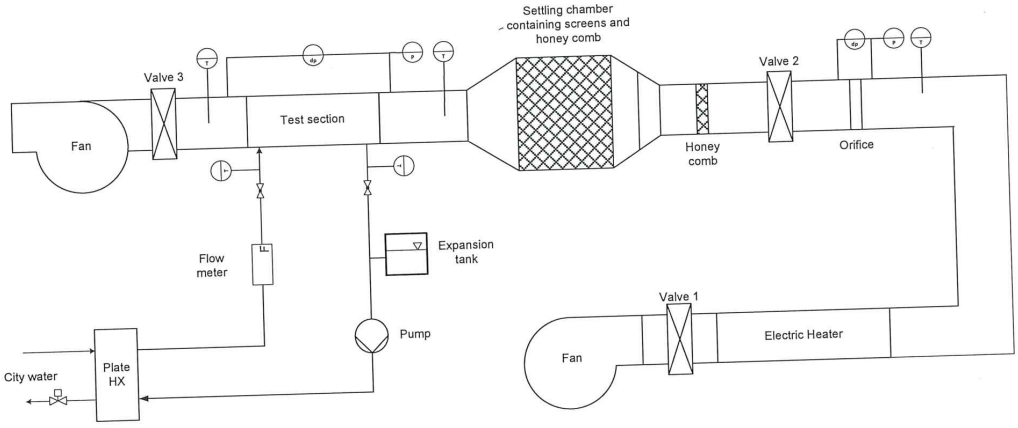

Figure 1: Schematic diagram

The schematic diagram of the experimental set-up is shown in Figure 1. The experimental rig is made-up of different parts interconnected by insulated steel pipes of cylindrical and rectangular cross-sections. The test rig consists of a fan, electric heater, orifice plate, flow conditioner, test section and instrumentation. The fan is used to maintain the required flow rate. The air then passes through the heating battery with a capacity of 450 kW where the air is heated up. The heating battery is switched off when temperature effect is not desired. The air flow rate is controlled by the fan speed. An orifice plate located 10 pipe diameter downstream of the value is used to estimate the flow rate (D = 300 mm). A combination of diverging (five pipe diameter upstream of the orifice plate) section, settling chamber (with screens and honeycomb) section and converging section (with contraction ratio of 7.5) are used to straightens the airflow and removes swirl and lateral velocity variations.

6 EVACUATION FROM THE EXPERIMENTAL AREA

Evacuate at signal from the alarm system or local gas alarms with its own local alert with sound and light outside the room in question, see 6.2

Evacuation from the rigging area takes place through the marked emergency exits to the assembly point, (corner of Old Chemistry Kjelhuset or parking 1a-b.)

Action on rig before evacuation:

- Stop the heating battery
- Shut off the air supply and the fan
- Close the rig valve –Valve
- Stop the glycol pump

7 WARNING

7.1 Before experiments

Send an e-mail with information about the planned experiment to:
Liste iept-experiments@ivt.ntnu.no

The e-mail should contain the following items:

- Name of responsible person:
- Experimental setup/rig:
- Start Experiments: (date and time)
- Stop Experiments: (date and time)

You must get the approval back from the laboratory management before start up. All running experiments are notified in the activity calendar for the lab to be sure they are coordinated with other activity.

7.2 Non-conformance

FIRE

If you are NOT able to extinguish the fire, activate the nearest fire alarm and evacuate area. Be then available for fire brigade and building caretaker to detect fire place.
If possible, notify:

NTNU	SINTEF
Morten Grønli, Mob: 918 97 515	Harald Mæhlum, Mob: 930 14 986
Terese Løvås: Mob: 918 97 007	Anne Karin T. Hemmingsen Mob: 930 19 669
NTNU – SINTEF Beredskapstelefon	800 80 388

GAS ALARM

If a gas alarm occurs, close gas bottles immediately and ventilate the area. If the level of the gas concentration does not decrease within a reasonable time, activate the fire alarm and evacuate the lab. Designated personnel or fire department checks the leak to determine whether it is possible to seal the leak and ventilate the area in a responsible manner.

PERSONAL INJURY

- First aid kit in the fire / first aid stations
- Shout for help
- Start life-saving first aid•

CALL 113 if there is any doubt whether there is a serious injury

OTHER NON-CONFORMANCE (AVVIK)

NTNU:
You will find the reporting form for non-conformance on:
https://innsida.ntnu.no/wiki/-/wiki/Norsk/Melde+avvik

SINTEF:
Synergi

8 ASSESSMENT OF TECHNICAL SAFETY

8.1 HAZOP

See Chapter 13 "Guide to the report template".

The experiment set up is divided into the following nodes:

Node 1	Main Test rig
Node 2	Cooling Circuit

Attachments: Form: Hazop_mal
Conclusion: (Safety taken care of)

8.2 Flammable, reactive and pressurized substances and gas

Are any flammable, reactive and pressurized substances and gases in use?

NO	

Attachments:
Conclusion: NA

8.3 Pressurized equipment

Is any pressurized equipment in use?

YES	Equipment have to undergo pressure testes in accordance with the norms and be documented

Attachments: (certificate for pressurized equipment)
Conclusion: Pressure test passed (see attachment B)

8.4 Effects on the environment (emissions, noise, temperature, vibration, smell)

Will the experiments generate emission of smoke, gas, odour or unusual waste?
Is there a need for a discharge permit, extraordinary measures?

NO	

Attachments:
Conclusion: NA

8.5 Radiation

See Chapter 13 "Guide to the report template".

NO	

Attachments:
Conclusion: NA

8.6 Chemicals

YES	Do a risk assessment of the use

Attachments: MSDS of Ethylenglycol

Conclusion: When working with Ethylenglycol, glasses and gloves should be worn. The concentration used in the test rig is 30% glycol and 70% water.
If your skin gets in contact with Ethylenglycol wash it with soap and water.
If your eyes get in contact with Ethylenglycol flush eyes for 15 Minutes with clean water and contact a doctor.

8.7 Electricity safety (deviations from the norms/standards)

NO	

Attachments:
Conclusion: NA

9 ASSESSMENT OF OPERATIONAL SAFETY

Ensure that the procedures cover all identified risk factors that must be taken care of. Ensure that the operators and technical performance have sufficient expertise.

9.1 Procedure HAZOP

The method is a procedure to identify causes and sources of danger to operational problems.
Attachments:: HAZOP_MAL_Prosedyre
Conclusion:

9.2 Operation and emergency shutdown procedure

Attachments: Procedure for running experiments

Emergency shutdown procedure:

- Stop the heating battery
- Shut off the air supply and the fan
- Close the rig valve –Valve
- Stop the glycol pump

9.3 Training of operators

Attachments: Training program for operators

9.4 Technical modifications

9.5 Personal protective equipment

- It is mandatory use of eye protection in the rig zone
- Use gloves when there is opportunity for contact with hot/cold surfaces.

9.5.1 *General Safety*

- Monitoring, can experiment run unattended, how should monitoring be?

Conclusion: The operator is allowed leaving the rig-area during the experiment, but only for a short period of 5 min

9.6 Safety equipment

- Warning signs, see the Regulations on Safety signs and signaling in the workplace
- Hot surfaces

9.7 Special precautions

10 QUANTIFYING OF RISK - RISK MATRIX

See Chapter 13 "Guide to the report template".
The risk matrix will provide visualization and an overview of activity risks so that management and users get the most complete picture of risk factors.

IDnr	Aktivitet-hendelse	Frekv-Sans	Kons	RV
	Fan noise	1	B	B1
	Much noise, people without protective gear enter the rig site	1	A	A1
	Barriers and running experiments outside working hours	1	A	A1
	Flow Temperature	2	B	B2
	Touching of hot surfaces	2	B	B2
	Contact with Ethylenglycol	2	B	B2

Conclusion: *Remaining risk found acceptable*

11 REGULATIONS AND GUIDELINES

Se http://www.arbeidstilsynet.no/regelverk/index.html

- Lov om tilsyn med elektriske anlegg og elektrisk utstyr (1929)
- Arbeidsmiljøloven
- Forskrift om systematisk helse-, miljø- og sikkerhetsarbeid (HMS Internkontrollforskrift)
- Forskrift om sikkerhet ved arbeid og drift av elektriske anlegg (FSE 2006)
- Forskrift om elektriske forsyningsanlegg (FEF 2006)
- Forskrift om utstyr og sikkerhetssystem til bruk i eksplosjonsfarlig område NEK 420
- Forskrift om håndtering av brannfarlig, reaksjonsfarlig og trykksatt stoff samt utstyr og anlegg som benyttes ved håndteringen
- Forskrift om Håndtering av eksplosjonsfarlig stoff
- Forskrift om bruk av arbeidsutstyr.
- Forskrift om Arbeidsplasser og arbeidslokaler
- Forskrift om Bruk av personlig verneutstyr på arbeidsplassen
- Forskrift om Helse og sikkerhet i eksplosjonsfarlige atmosfærer
- Forskrift om Høytrykksspyling
- Forskrift om Maskiner
- Forskrift om Sikkerhetsskilting og signalgivning på arbeidsplassen
- Forskrift om Stillaser, stiger og arbeid på tak m.m.
- Forskrift om Sveising, termisk skjæring, termisk sprøyting, kullbuemeisling, lodding og sliping (varmt arbeid)
- Forskrift om Tekniske innretninger
- Forskrift om Tungt og ensformig arbeid
- Forskrift om Vern mot eksponering for kjemikalier på arbeidsplassen (Kjemikalieforskriften)
- Forskrift om Vern mot kunstig optisk stråling på arbeidsplassen
- Forskrift om Vern mot mekaniske vibrasjoner
- Forskrift om Vern mot støy på arbeidsplassen

Veiledninger fra arbeidstilsynet
se: http://www.arbeidstilsynet.no/regelverk/veiledninger.html

12 DOCUMENTATION

- Tegninger, foto, beskrivelser av forsøksoppsetningen
- Hazop_mal
- Sertifikat for trykkpåkjent utstyr
- Håndtering avfall i NTNU
- Sikker bruk av LASERE, retningslinje
- HAZOP_MAL_Prosedyre
- Forsøksprosedyre
- Opplæringsplan for operatører
- Skjema for sikker jobb analyse, (SJA)
- Apparaturkortet
- Forsøk pågår kort

13 GUIDANCE TO RISK ASSESSMENT TEMPLATE

Chapter 7 Assessment of technical safety.

Ensure that the design of the experiment set up is optimized in terms of technical safety. Identifying risk factors related to the selected design, and possibly to initiate re-design to ensure that risk is eliminated as much as possible through technical security.
This should describe what the experimental setup actually are able to manage and acceptance for emission.

7.1 HAZOP

The experimental set up is divided into nodes (eg motor unit, pump unit, cooling unit.). By using guidewords to identify causes, consequences and safeguards, recommendations and conclusions are made according to if necessary safety is obtained. When actions are performed the HAZOP is completed.
(e.g. "No flow", cause: the pipe is deformed, consequence: pump runs hot, precaution: measurement of flow with a link to the emergency or if the consequence is not critical used manual monitoring and are written into the operational procedure.)

7.2 Flammable, reactive and pressurized substances and gas.

According to the Regulations for handling of flammable, reactive and pressurized substances and equipment and facilities used for this:

Flammable material: Solid, liquid or gaseous substance, preparation, and substance with occurrence or combination of these conditions, by its flash point, contact with other substances, pressure, temperature or other chemical properties represent a danger of fire.
Reactive substances: Solid, liquid, or gaseous substances, preparations and substances that occur in combinations of these conditions, which on contact with water, by its pressure, temperature or chemical conditions, represents a potentially dangerous reaction, explosion or release of hazardous gas, steam, dust or fog.
Pressurized : Other solid, liquid or gaseous substance or mixes having fire or hazardous material response, when under pressure, and thus may represent a risk of uncontrolled

emissions

Further criteria for the classification of flammable, reactive and pressurized substances are set out in Annex 1 of the Guide to the Regulations "Flammable, reactive and pressurized substances"
http://www.dsb.no/Global/Publikasjoner/2009/Veiledning/Generell%20veiledning.pdf
http://www.dsb.no/Global/Publikasjoner/2010/Tema/Temaveiledning_bruk_av_farlig_stoff_Del_1.pdf

Experiment setup area should be reviewed with respect to the assessment of Ex zone
- Zone 0: Always explosive atmosphere, such as inside the tank with gas, flammable liquid.
- Zone 1: Primary zone, sometimes explosive atmosphere such as a complete drain point
- Zone 2: secondary discharge could cause an explosive atmosphere by accident, such as flanges, valves and connection points

7.4 Effects on the environment

With pollution means: bringing solids, liquid or gas to air, water or ground, noise and vibrations, influence of temperature that may cause damage or inconvenience effect to the environment.
Regulations: http://www.lovdata.no/all/hl-19810313-006.html#6
NTNU guidance to handling of waste:http://www.ntnu.no/hms/retningslinjer/HMSR18B.pdf

7.5 Radiation

Definition of radiation

Ionizing radiation: Electromagnetic radiation (in radiation issues with wawelength <100 nm) or rapid atomic particles (e.g. alpha and beta particles) with the ability to stream ionized atoms or molecules.
Non ionizing radiation: Electromagnetic radiation (wavelength >100 nm), og ultrasound[1] with small or no capability to ionize.
Radiation sources: All ionizing and powerful non-ionizing radiation sources.
Ionizing radiation sources: Sources giving ionizing radiation e.g. all types of radiation sources, x-ray, and electron microscopes.
Powerful non ionizing radiation sources: Sources giving powerful non ionizing radiation which can harm health and/or environment, e.g. class 3B and 4. MR_2 systems, UVC_3 sources, powerful IR sources[4].
[1]Ultrasound is an acoustic radiation ("sound") over the audible frequency range (> 20 kHz). In radiation protection regulations are referred to ultrasound with electromagnetic non-ionizing radiation. [2]MR (e.g. NMR) - nuclear magnetic resonance method that is used to "depict" inner structures of different materials. [3]UVC is electromagnetic radiation in the wavelength range 100-280 nm. [4]IR is electromagnetic radiation in the wavelength range 700 nm - 1 mm.

For each laser there should be an information binder (HMSRV3404B) which shall include:
- General information
- Name of the instrument manager, deputy, and local radiation protection coordinator
- Key data on the apparatus
- Instrument-specific documentation

- References to (or copies of) data sheets, radiation protection regulations, etc.
- Assessments of risk factors
- Instructions for users
- Instructions for practical use, startup, operation, shutdown, safety precautions, logging, locking, or use of radiation sensor, etc.
- Emergency procedures
- See NTNU for laser: http://www.ntnu.no/hms/retningslinjer/HMSR34B.pdf

7.6 The use and handling of chemicals.

In the meaning chemicals, a element that can pose a danger to employee safety and health
See: http://www.lovdata.no/cgi-wift/ldles?doc=/sf/sf/sf-20010430-0443.html
Safety datasheet is to be kept in the HSE binder for the experiment set up and registered in the database for chemicals.

Chapter 8 Assessment of operational procedures.

Ensures that established procedures meet all identified risk factors that must be taken care of through operational barriers and that the operators and technical performance have sufficient expertise.

8.1 Procedure Hazop

Procedural HAZOP is a systematic review of the current procedure, using the fixed HAZOP methodology and defined guidewords. The procedure is broken into individual operations (nodes) and analyzed using guidewords to identify possible nonconformity, confusion or sources of inadequate performance and failure.

8.2 Procedure for running experiments and emergency shutdown.

Have to be prepared for all experiment setups.
The operating procedure has to describe stepwise preparation, startup, during and ending conditions of an experiment. The procedure should describe the assumptions and conditions for starting, operating parameters with the deviation allowed before aborting the experiment and the condition of the rig to be abandoned.
Emergency procedure describes how an emergency shutdown have to be done, (conducted by the uninitiated),
what happens when emergency shutdown, is activated. (electricity / gas supply) and
which events will activate the emergency shutdown (fire, leakage).

Chapter 9 Quantifying of RISK

Quantifying of the residue hazards, Risk matrix
To illustrate the overall risk, compared to the risk assessment, each activity is plotted with values for the probability and consequence into the matrix. Use task IDnr.
Example: If activity IDnr. 1 has been given a probability 3 and D for consequence the risk value become D3, red. This is done for all activities giving them risk values.
In the matrix are different degrees of risk highlighted in red, yellow or green. When an activity ends up on a red risk (= unacceptable risk), risk reducing action has to be taken

CONSEQUENSES						
	Svært alvorlig	E1	E2	E3	E4	E5
	Alvorlig	D1	D2	D3	D4	D5
	Moderat	C1	C2	C3	C4	C5
	Liten	B1	B2	B3	B4	B5
	Svært liten	A1	A2	A3	A4	A5
		Svært liten	Liten	Middels	Stor	Svært Stor
		PROBABILITY				

The principle of the acceptance criterion. Explanation of the colors used in the matrix

Colour		Description
Red		Unacceptable risk Action has to be taken to reduce risk
Yellow		Assessment area. Actions has to be considered
Green		Acceptable risk. Action can be taken based on other criteria

Thomas Ivelt Utstein

Aspects of Flow and Heat Transfer in Finned Tube Bundles.

NTNU
Norwegian University of
Science and Technology